ORIGINAL RESEARCH ARTICLE

Development and Design of the First Industrial Magnetohydrodynamic Slag-Cleaning Reactor From Execution and Analysis of Pilot Plant Tests Through Coupled CFD Simulations

MICHAEL KALISCH, BERND FRIEDRICH, and MARKUS A. REUTER

The future challenge for copper smelters is to increase metal yield by reducing copper losses and valorizing the slag as a marketable by-product. This can be achieved through further slag cleaning in a conventional submerged arc furnace (SAF) where remaining metallic oxides are reduced, and metal droplets have more settling time. Nevertheless, a significant amount of copper matte and metallic copper is still present as slight inclusions that cannot settle through the slag layer under simple gravity after SAF treatment. This work presents the development of a new industrial type of slag-cleaning concept, based on the magnetohydrodynamic (MHD) principle, that can be coupled downstream of conventional slag-cleaning technology (*e.g.*, electric reduction furnace). The cleaning efficiency and operating conditions were evaluated in several pilot test campaigns using a SAF supplemented by an externally applied magnetic field (electromagnet), which interacts with electrodes generating Lorentz forces, which are responsible for an MHD stirring effect. In order to simulate experimental conditions and thus understand reaction kinetics and settle mechanisms during pilot tests, this work includes computational fluid dynamics (CFD) models. In order to represent these electromagnetic conditions, the focus of this work is to develop a new coupled CFD model. Numerical simulations showed the interactions between MHD flow field, slag properties, and metal recovery in an industrial slag-cleaning reactor and demonstrated the MHD cleaning effect on non-ferrous slags.

https://doi.org/10.1007/s11663-023-02758-9

I. INTRODUCTION

A large proportion of the metals produced worldwide today are obtained by metallurgical smelting. Process efficiency is limited by the physical and thermochemical equilibrium between molten metal and the slag phase, so some of the valuable metals in the starting material are lost in the slag.

Metallurgical processes and current plant concepts do not permit a complete recovery of valuable metals (*e.g.*, copper, nickel, cobalt, molybdenum, antimony, zinc, and tin) from the slag phase of metal production. Selective separation and metal enrichment of these elements can improve the valuable metal potential. At the same time, preserving raw materials by enhancing the efficiency of existing processes would bring environmental benefits thanks to the potential slag reuse as secondary construction material.[1,2]

SMS group GmbH, a leading plant manufacturer in the field of metallurgical technology, the Institute for Metallurgical Process Technology and Metal Recycling of RWTH Aachen University, the Department of Mining Engineering at the Universidad de Chile, and Aurubis AG in Hamburg have developed a new type of slag-cleaning concept that can be installed downstream of conventional slag-cleaning systems (*e.g.*, electric reduction furnace).[3]

The new process known as the ''slag washing machine'' is based on a conventional rectangular slag-cleaning furnace with two well-differentiated zones corresponding to the physical phenomena that occur

MICHAEL KALISCH and MARKUS A. REUTER are with the SMS Group GmbH, Eduard-Schloemann-Straβe 4, 40237 Düsseldorf, Germany. Contact e-mail: michael.kalisch@sms-group.com BERND FRIEDRICH is with the IME Process Metallurgy and Metal Recycling, RWTH Aachen University, Intzestr, 52072 Aachen, Germany.

Manuscript submitted September 28, 2022; accepted February 16, 2023.

Article published online March 24, 2023.

there. In the first inlet zone, the molten slag is stirred by means of the magnetohydrodynamic effect, resulting in the coagulation of small matte and metal droplets. Droplets sink into the matte phase in the rear second zone, driven by a direct current (DC) field and by gravity.[4,5]

The furnace design of the first industrial magnetohydrodynamic 100 t/h copper slag processing plant presented in this work is shown in Figure 1.

As part of the "Innovative Technologies for Resource Efficiency—Raw Material Intensive Production Processes" funding initiative* run by the German Federal Ministry of Education and Research (BMBF), this concept is further developed into an efficient and flexible process to treat copper slags from primary metal production. The goal is to maximize the recovery yield of valuable metals (mainly copper) compared to established processes.[3]

*Project name: Prevention of Metal Losses in Metallurgical Slags Using the Example of Copper Extraction; Funding codes: BMBF 033R006B; Funding program: Innovative Technologies for Resource Efficiency—Raw Material Intensive Production Processes.

The study presented in this article describes the development of this technology from its metallurgical fundamentals to the final first industrial application in an industrial MHD copper slag processing plant. This work also includes lab-scale and pilot trials on a scale of 4 t/h at Aurubis AG in Hamburg and is complemented by the development of MHD flow models. For this purpose, coupled flow simulations are performed using the ANSYS program (EMAG) for calculating the magnetic and electric fields and FLUENT software for flow calculation.

Four sequential analysis steps shown in Figure 2 are required to develop the first industrial magnetohydrodynamic copper slag processing system.

Step (a) Assessing process parameters from two pilot plants to determine industrial operating conditions;

Step (b) Analyzing mass and heat balances to determine and extrapolate material flows as well as melting performance;

Step (c) Setting up a coupled CFD simulation model to determine the optimal magnetic field alignment as a function of energy input, matched to the industrial reactor geometry;

Step (d) Correlating industrial furnace dimensions using comparative studies with existing rectangular copper slag-cleaning furnaces and determining energy consumption.

For the industrial-type reactor design, the conventional reduction furnace (SAF) for slag cleaning has to be supplemented by an externally applied magnetic field (electromagnet). By interacting with the electrode current, an "artificial" Lorentz force is generated, which is responsible for the magnetohydrodynamic stirring effect in the bath and has never before been investigated for industrial slag treatment to the extent presented in this work.

The combined use of electric current sources and axial magnetic fields is a well-known effect in metallurgy for generating swirling MHD flows, and their physical principles are described in detail.[6] The magnetohydrodynamic phenomena can be differentiated into two very different groups depending on the intensity of applied current and axial external magnetic field. Low electric currents (< 10 A) and high magnetic fields (> 0.1 T) in fluids represent the first group.[7,8]

The study by Messadek *et al.*[9] covered a wide range of current and intensive axial magnetic fields of up to 6 Tesla. Sommeria *et al.*[10,11] injected low current in a thin liquid mercury layer in the presence of external axial magnetic field, comparable to our outer magnet system.

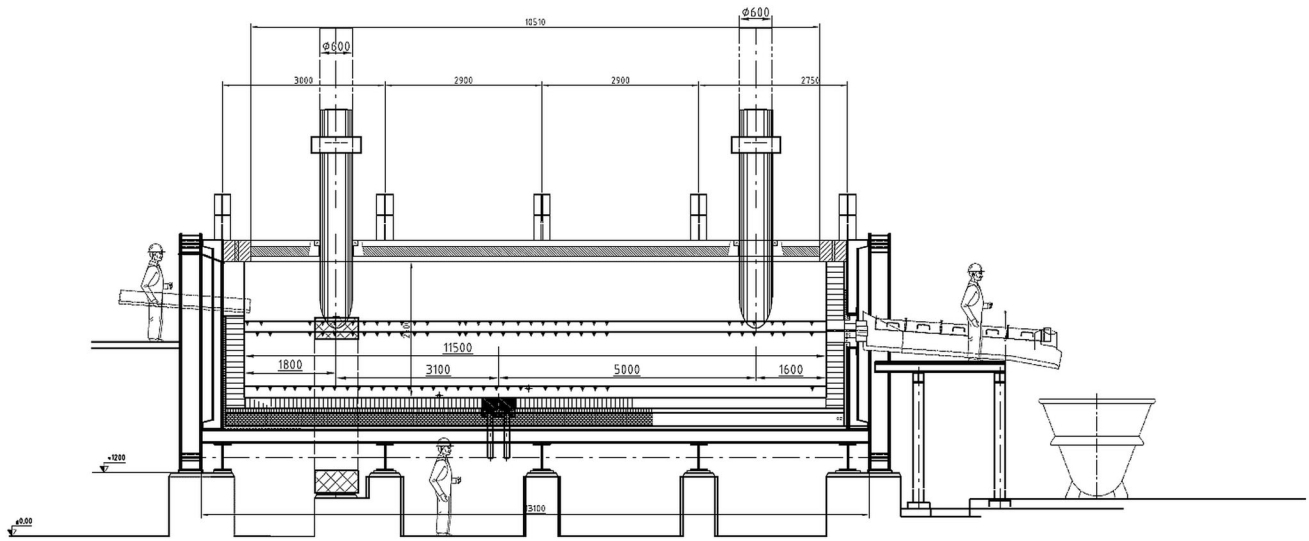

Fig. 1—Furnace design for a 100 t/h industrial magnetohydrodynamic copper slag-cleaning reactor.

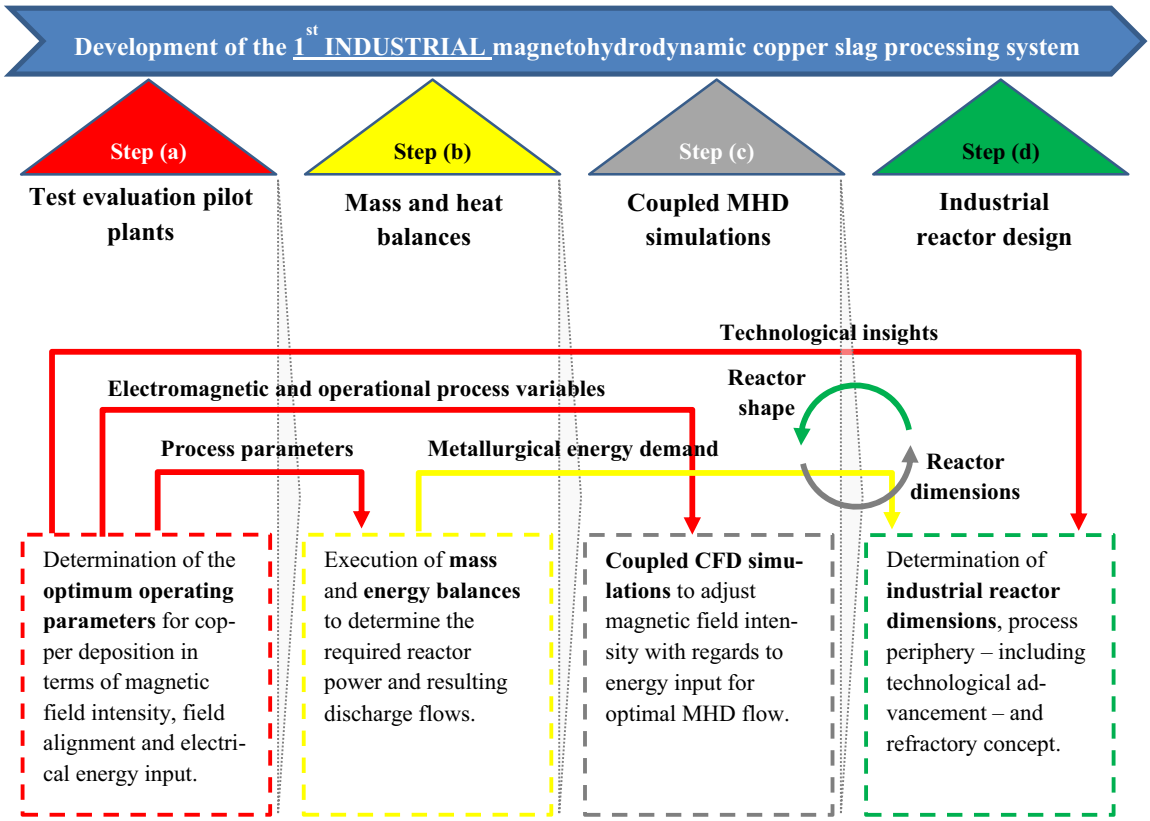

Fig. 2—Analysis steps for the design of the first industrial magnetohydrodynamic slag-cleaning reactor.

Due to the high magnetic flux density in the fluids, these studies have no relevance for our application. The second group focuses on strong current (> 100 A) and low magnetic field (< 10 mT), with metallurgical domain processes that include electroslag remelting[12] and electric arc furnaces.[13,14] In these processes, electrode currents of up to 100 kA are used, resulting in MDH flow effects in the liquid melt, generated by Lorentz forces from the interaction between the electric current and its self-magnetic field. Depending on the medium and the electric current density, these forces can cause negligible secondary flows up to potent electro-vortex flow (EVF). Liu *et al.*[15] compared experimental measurements of an EVF by means of simulations. Good match was achieved only if small axial magnetic field was assumed to be present. The study concluded that external magnetic fields alter and suppress the flow as the field increases. This mechanism of poloidal electro-vortical flow suppression in an electro-vortex flow has been verified in a liquid metal experiment performed by Kolesnichenko *et al.*.[16]

Numerous authors such as Choudhary and Szekely,[17] Jardy *et al.*,[18] and especially Sheng *et al.*[19,20] have investigated the magnetohydrodynamic effect on non-ferrous slags. These studies showed that this magnetohydrodynamic stirring effect generated by the electrode current in conventional slag reduction furnaces is negligible compared to the natural convection flow. In this context, computational fluid dynamic (CFD) simulation models for a six-in-line (36 MVA furnace for smelting nickel calcine) furnace have also been developed by Gunnewiek and Tullies,[21,22] Sheng, Irons, and Tisdalle[20] and the CSIR (Council for Scientific and Industrial Research)[23] in South Africa for the Polokwane furnace. Sheng *et al.* found that electromagnetic stirring force is 1 pct of the natural convection and bubble-driven forces.[20]

Nevertheless, the previous models for the conventional electric reduction furnace do not consider the influence of "artificially" generated magnetohydrodynamic flow by an external induced magnetic field. This effect and its interaction with the electrode current density are analyzed in detail to design the first industrial MHD copper slag-cleaning process. First, CFD simulations related to the pilot tests were performed using COMSOL® (FEMLAB). These models did not generate the magnetic field directly from the external magnet—it was only artificially remodeled.[5]

Pilot trials using the magnetohydrodynamic effect have also been carried out for product homogenization in the glass industry by Krieger, Hülsenberg and Thess,[24,25] which, together with the CFD simulation results from Giessler[26] and Cepite,[27] provide some guidance for the CFD studies developed here. Perez[28] continued on this work and investigated the usability of Lorentz forces in a coloring forehearth of molten glass tanks to improve its performance.

The CFD simulation results, together with the experimental research results, enabled the development of the scientific functional chain "electromagnetic field—MHD flow field—slag properties—metal recovery" in an industrial slag-cleaning reactor and, consequently, the investigation of the physical principles of the MHD cleaning effect on non-ferrous slags types.

II. MAGNETOHYDRODYNAMIC COPPER SLAG CLEANING

A. *Copper Slag Cleaning in a DC Furnace with Crossed Electromagnetic Fields*

Typical pyrometallurgical slag cleaning in a conventional submerged arc furnace (SAF) usually involves heating the slag, reducing oxides, and settling matte and metal droplets. Heating the slag decrease viscosity and accelerates reactions. Magnetite (Fe_3O_4) reduction releases copper inclusions and facilitates the reduction of other dissolved metal oxides.[4] A significant amount of copper matte and metallic copper is present as minor inclusions (on a scale of 3 to 50 μm) that cannot settle through the slag layer under simple gravity. Additional coalescence is required to remove the matte and metallic inclusions from the slag and to increase the overall yield. However, two key factors have to be considered: high surface tension of copper matte and metal droplets and the relatively slow slag bath movement.[4,5]

The new slag-cleaning concept combines a DC rectangular furnace (see Figure 1) with an externally induced magnetic field, as illustrated in Figure 3.

Intensive slag stirring increases the probability of coagulation (= agglomeration of particles) and coalescence (= confluence of emulsion droplets), promoting an enhanced mass transfer and reduction kinetics (coke) and destabilizing the emulsion of copper matte and metal inclusions.

Suppose the plane of vectors of electric and magnetic fields is perpendicular to the gravity vector, as depicted in Figure 3, then the application of a DC field with the superimposed permanent magnetic field, in combination with the conventional AC slag reduction furnace, would generates the following electrochemical and magnetohydrodynamic effects in the slag phase:

1. Joule's heat generation[5,29,30]
2. Magnetite and cuprous oxide reduction on the coke/slag interface[31–33]
3. Acceleration of magnetite and cuprous oxide reduction due to MHD slag stirring[5]
4. Increased formation of larger droplets due to collision in the MHD flow area[29,30,34]
5. Acceleration of inclusions settling by electrocapillary motion phenomena[35,36]
6. Slag electrolysis with magnetite reduction and copper cathodic precipitation[30]
7. Gravitational coalescence and settling of matte inclusions[5,37,38]

B. *Relevant Test Results Used for the Industrial Furnace Design*

Over the last two decades, numerous fundamental tests, CFD modeling, and pilot-scale tests have been carried out. In the initial phase of the project, a mathematical model of gravitational coalescence

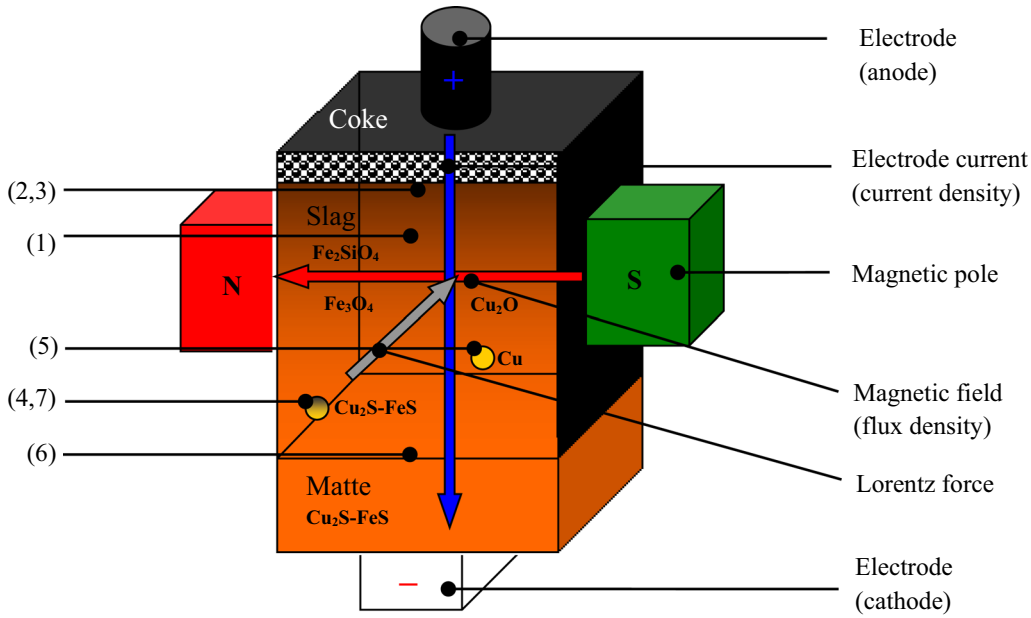

Fig. 3—Electromagnetic fields and resulting Lorentz force in a liquid copper slag phase.

combined with forced slag motion showed the effective removal of copper matte inclusions from the slag. Preliminary results in laboratory pilot-scale tests on continuous slag cleaning showed fast slag reduction and confirmed the improved metal removal from the slag.[5]

Additionally, pilot tests (1 to 2 t/h of slag charge) were carried out at the Anglo American plant in Chagres, Chile, demonstrating the successful functioning of the process principles. The chemical analysis in Figure 4 confirmed that the initial copper content of 1.6 pct in the slag was reduced to below 0.7 pct. In addition, the magnetite content in Figure 5 decreased from 14 to 8 pct, thereby showing a clear correlation between the copper and magnetite content. Re-polarization of the magnet did not allow any conclusions to be made regarding the slag behavior.[39,40]

These test results encouraged SMS group to proceed with the test work on a 4 t/h pilot plant. The pilot plant in Hamburg at Aurubis AG was operated over ten campaigns. During the operating period, the furnace was fed semi-continuously with slag from the industrial slag-cleaning furnace using a crane with specially constructed ladles. Figure 6(a) shows a 3D sketch of the entire plant with pilot scale operation in Figure 6(b).

The test work in the pilot plant campaigns covered ten test weeks over two years, starting in March 2010. The time gap between each campaign was required to evaluate and determine the results thus obtained and to make necessary changes and improvements to the pilot plant design.

The key question in the new electrodynamic slag-cleaning concept is the velocity distribution of the slag phase induced by crossing the electric and magnetic fields. Parallel to test trials in the pilot plant in Hamburg, the results were evaluated by means of CFD simulations. One of the major challenges was modeling the entire unit's electromagnetic field because the field's intensity and direction greatly influence the reactor's flow pattern. Correlations between simulations and experimental work elucidated the relevant parameters utilized in the trial campaign.

For this reason, several series of measurements were carried out to determine the magnetic field pattern, shown in Figure 7(a). Following completion of the magnet, the field tests shown below confirmed the FEM simulation results shown in Figure 7(b). Flux density measurements with a magnet coil current of 30 A (= 30,000 A-turns) demonstrated the desired 200 Gauss (= 0.02 Tesla) in the center.

As shown in Figure 7(b), magnetic field measurements in all air-gap planes showed a symmetry behavior to the third power, which also matched the simulation results. Magnetic material properties such as the saturation curve of the magnetic iron core in Figure 8 and solver settings in Section IV–B are used for a further CFD study for tuning the magnetic field intensity in the industrial MHD reactor.

Figure 8(b) shows the highest achievable polarization of the magnetic iron core, which is thus within saturation range, from a magnetic field intensity of approx. 7940 A/m; the permeability of $\mu = 2.78 \times 10^{-4}$ Vs/Am.

The resulting magnetic field expands hemispherically in the reactor (slag, coke, and matte), as shown in Figure 9(a). To ensure optimal field intensity for the MHD effect, the orientation of the magnetic poles is aligned with the electrode tip position in the coke/slag interface (see Figure 9(b)).

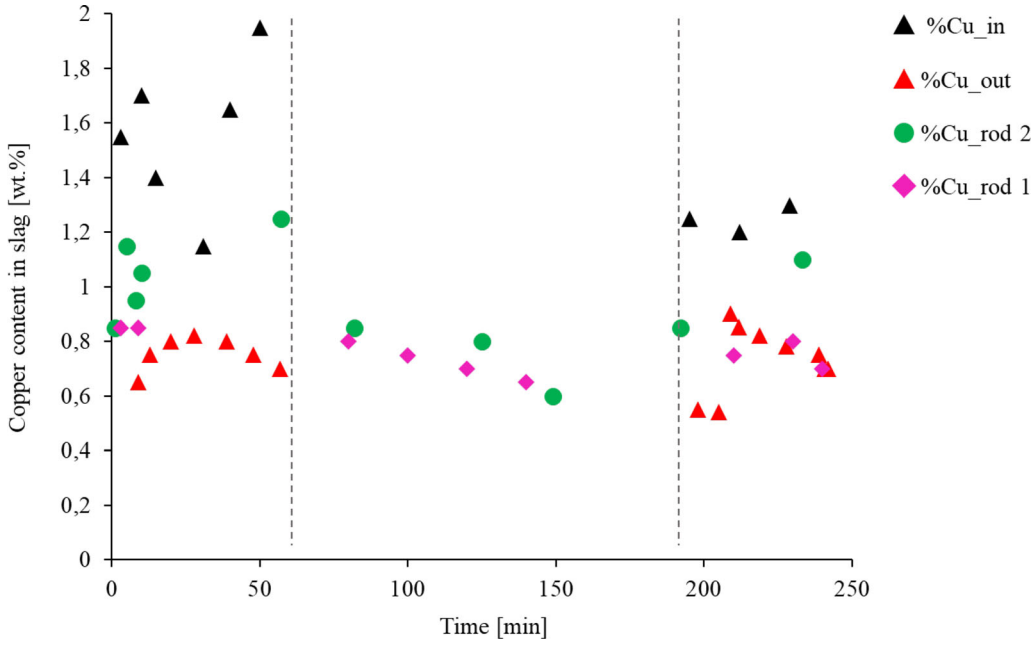

Fig. 4—Copper content in slag over time: (pct *Cu_in*) spoon samples of charged slag; (pct *Cu_out*) spoon samples of slag tapped out; (pct *Cu_rod 1*) slag samples by dip rod close to electrode; (pct *Cu_rod 2*) slag samples by dip rod close to outlet.

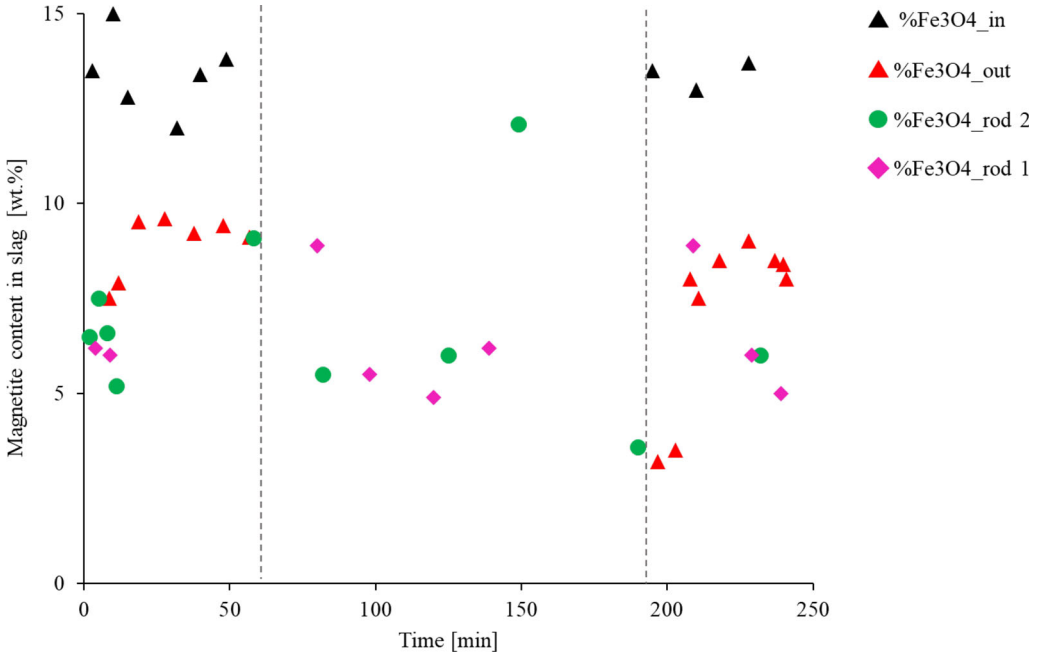

Fig. 5—Magnetite content in slag over time: (pct *Fe3O4_in*) spoon samples of charged slag; (pct *Fe3O4_out*) spoon samples of slag tapped out; (pct *Fe3O4_rod1*) slag samples by dip rod close to electrode; (pct *Fe3O4_rod2*) slag samples by dip rod close to outlet.

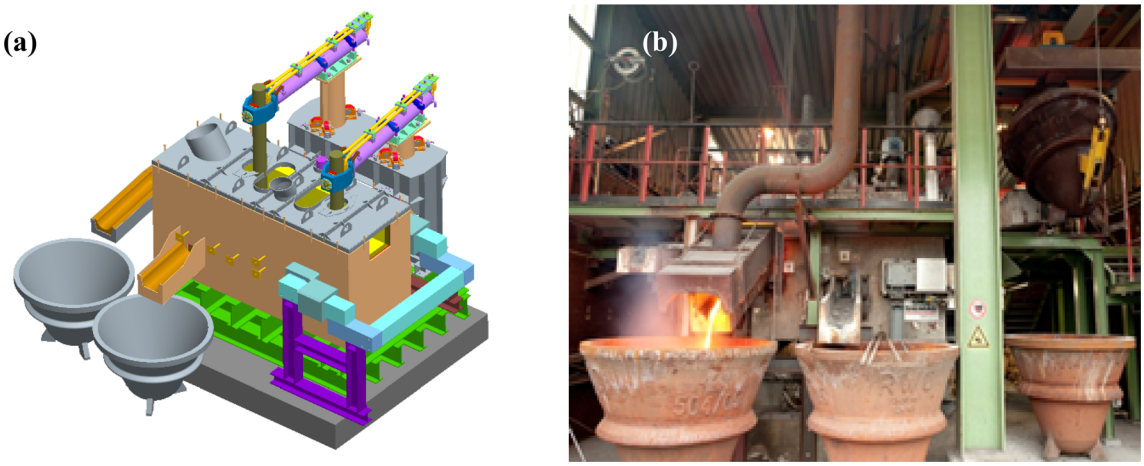

Fig. 6—(*a*) 3D-sketch of the entire plant and (*b*) pilot scale operation.

In order to evaluate the relative efficiency of copper separation in the pilot plant, a comparison with a reference state without magnetic stirring was necessary. Except for the last of ten campaigns carried out, all included a period of slag treatment in the pilot reactor without magnetic stirring.

As shown in Figure 10, even at a high copper concentration (> 1.00 wt pct CuIN) in the feed material, enhanced copper separation was observed, just as it was for low concentrations (≤ 0.65 wt pct CuIN). Results show that the magnetic field application increases 1.5 times the cleaning process.[41,42]

Obtained results lead to further questions regarding the impact of operating parameters on the industrial application and represent our analysis step (a) in Figure 2. Several parameters such as temperature, magnetite content, slag basicity, besides others, were taken into account. However, one main influencing factor remains—the copper concentration of the inlet slag. As a result, Table I shows the most significant series of experiments in campaign VI to IX with the main magnet settings, electrode power ratio and the corresponding average copper contents in the inlet and overflow.

From this it can be deduced that a reversed-polarity magnetic field with a coil current of 16 A and pulsating clocking achieved the best copper separation. In terms of power distribution between the electrodes, the ratio 100:0 or 90:10 has proven successful, with the challenge here being to avoid buildup in the slag overflow area (electrode 2). With respect to the settling behavior of the coagulated copper inclusions, a residence time of less

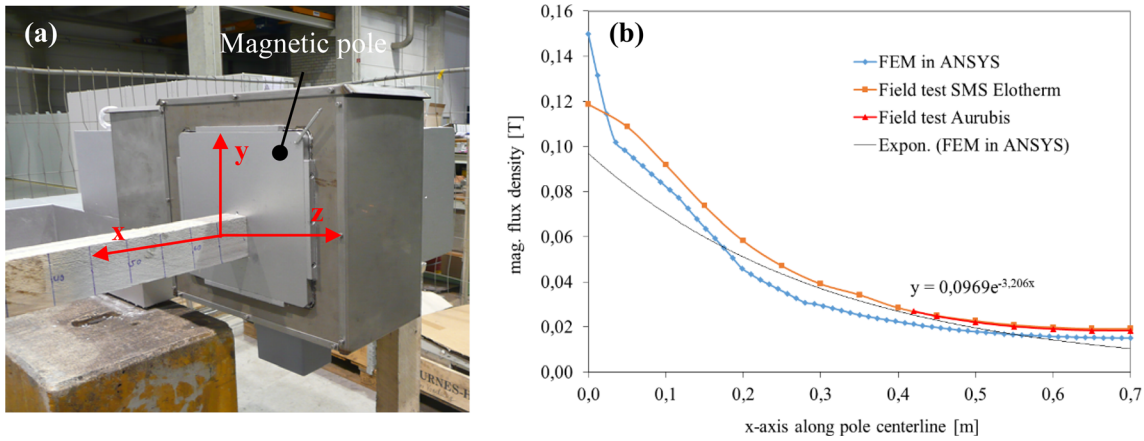

Fig. 7—(*a*) Magnet test rig at the SMS Elotherm and (*b*) mag. flux density measurement results compared to FEM calculation with 30,000 A-turns.

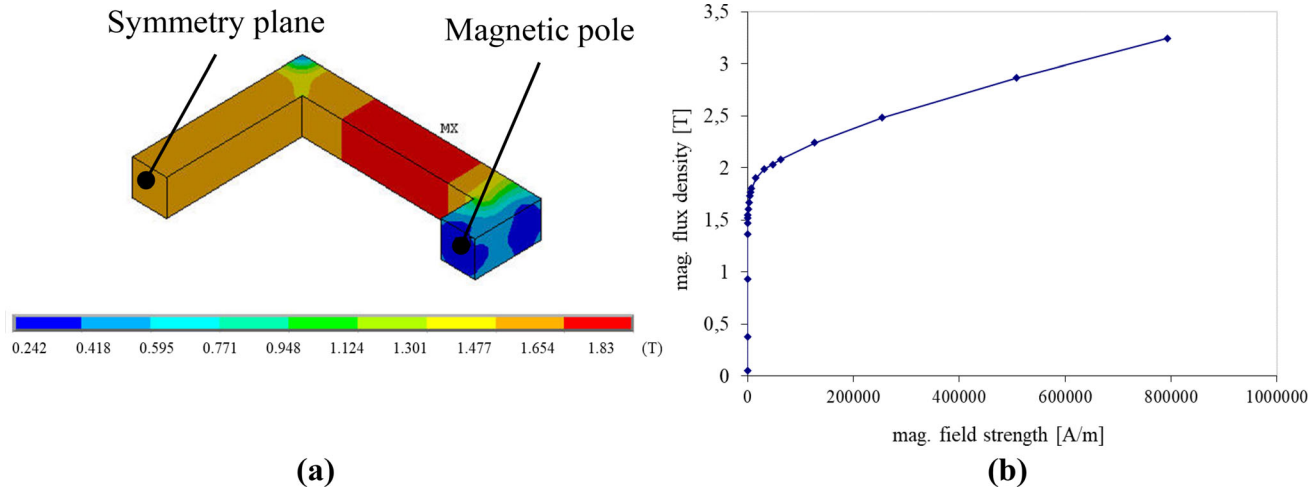

Fig. 8—(*a*) ANSYS simulation result for mag. flux density in the pilot magnet system and (*b*) corresponding B-H curve for the iron core.

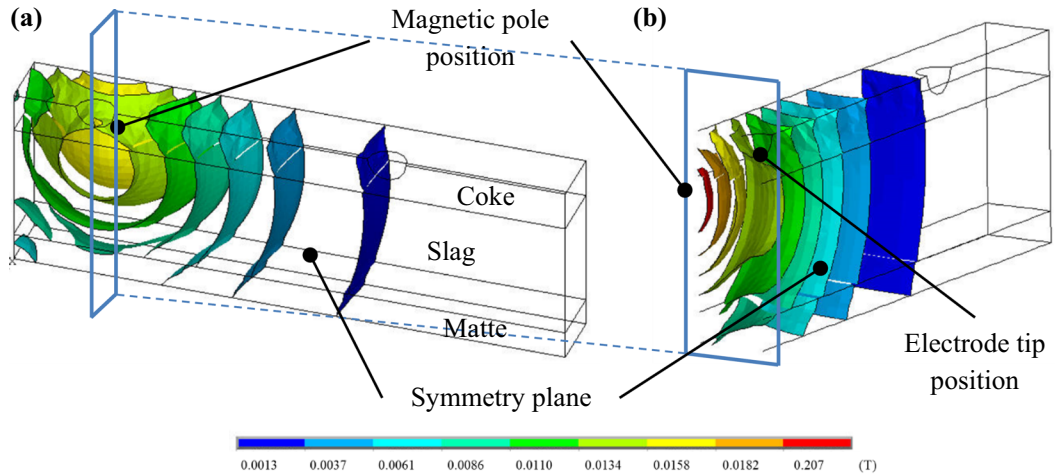

Fig. 9—ANSYS simulation result for mag. flux density distribution in reactor: (*a*) overall view to symmetry plane and (*b*) section view at electrode and magnetic pole position.

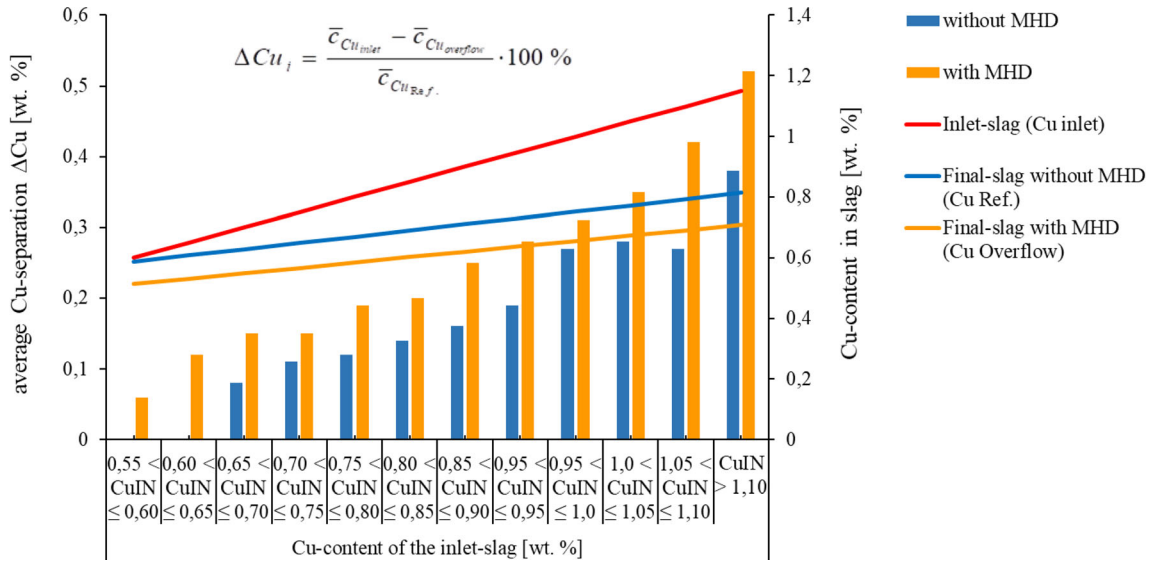

Fig. 10—Comparison of copper separation and copper content in the final slag with and without enhanced magnetohydrodynamic stirring, depending on the copper concentration of the feed material.

than 30 minutes has been found to be a deterioration. As shown in Figure 2, for the CFD study these results of magnetic field alignment and power distribution are used for adjusting the magnetic field strength as well as for determining the reactor power for industrial use. The additional task in this context is to improve and increase the efficiency of the magnetohydrodynamic stirring effect by the magnet based on the industrial furnace geometry, which will be investigated in the next section.

III. INDUSTRIAL MHD-SLAG-CLEANING REACTOR

A. *Mass and Energy Balance*

As shown in analysis step (b) in Figure 2, the basic operating parameters of the industrial furnace require process-based mass and heat balances and the determination of the factors influencing these various process parameters: Heat losses, electrical power input, gas volume and temperature for different slag output temperatures, magnetite contents and slag throughputs. Based on individual test campaigns and to attain the maximum possible flexibility for industrial use, an inlet temperature range of 1170 °C to 1270 °C and a slag throughput of between 40 and 140 t/h (with an average slag throughput of 100 t/h) are used for balancing. The chemical composition of the slag corresponds to the input data from the tests in Hamburg; an input magnetite content of Fe_3O_4 = 3 pct and total copper content of Cu = 0.82 pct are estimated for the balances. The heat generated and consumed by the following reactions determine the temperature distribution in the reactor and the rate of oxide reduction[29–31,43–45]:

$$[Fe_3O_4]_{slag}+C = 3[FeO]_{slag}+\{CO\}_{gas} \quad [1]$$

$$[Cu_2O]_{slag}+C = 2(Cu)_{metal}+\{CO\}_{gas} \quad [2]$$

$$\{O_2\}_{air}+C = \{CO\}_{gas} \quad [3]$$

$$\{CO_2\}_{gas}+C = 2\{CO\}_{gas} \quad [4]$$

$$[Fe_3O_4]_{slag}+\{CO\}_{gas} = 3[FeO]_{slag}+\{CO_2\}_{gas} \quad [5]$$

$$[Cu_2O]_{slag}+\{CO\}_{gas} = 2(Cu)_{metal}+\{CO_2\}_{gas} \quad [6]$$

$$\{O_2\}_{air}+2\{CO\} = 2\{CO_2\}_{gas} \quad [7]$$

Based on the pilot results from Hamburg, it is assumed for the balances that 20 pct of copper is present as dissolved Cu_2O and 80 pct as Cu_2S, which is partly dissolved and partly in the form of copper matte inclusions with a size of 5 to 200 μm. The destabilization of matte emulsion requires the intense MHD slag motion. During this movement, collisions between inclusions become more likely, and the inclusions themselves increase in mass and diameter and begin to settle faster. Dissolved copper as Cu_2O is reduced to metallic copper. The reduction of cuprous oxide starts when the concentration of magnetite is below 5 pct and is determined by the equilibrium of the following reaction[33,46]:

Table I. Test Results in Campaign VI to IX for Copper Separation for Different Power Distributions and Magnetic Field Settings

Campaign	Power [P] El.1:El.2	Setting Magnet Current [I], Clocking [s]	Inlet Cu [Wt Pct]	Outlet Cu [Wt Pct]
VI	70:30	IMagnet = 32 A	0.81	0.69
		IMagnet = 16 A	0.81	0.59
		Pulsating	0.84	0.51
		Alternate	0.80	0.54
VII	70:30	Reference	0.83	0.69
		Pulsating	0.82	0.62
VIII	70:30	Reference	1.04	0.84
		Clocking 60/10 s	1.13	0.76
		Clocking 30/10 s	1.04	0.68
		Slag temperature 1300 °C	0.95	0.66
IX	90:10	Clocking 30/10 s	0.71	0.52
	100:0	Clocking 30/10 s	0.70	0.49
	100:0	Clocking 30/10 s; Ret. time < 30 min	0.73	0.63
	100:0	Clocking 2/4 s	0.73	0.53
	100:0	Clocking 2/4 s	0.73	0.50
	70:30	Clocking 2/4 s	0.73	0.50

$$3[FeO]_{slag}+[Cu_2O]_{slag}= [Fe_3O_4]_{slag}+2(Cu)_{metal} \quad [8]$$

The composition of the final slag, also based upon the results of the same test campaign VII (Table II] and the phase diagram is calculated. Due to the differentiated heat transfer in the gas and slag phases, the mass and heat balances are split into two combined balances: Condensed phases (matte, slag, coke) with refractory material below the coke surface and the gaseous phase above the coke surface with the furnace roof and associated side walls.

Heating the input slag and reducing the entry magnetite content require the largest amount of energy needs. The maximum fluctuations in the average slag inlet temperatures in Hamburg were within the 1170 °C to 1270 °C range, due to the ladle transport from the existing slag-cleaning furnace. Therefore, a variable slag inlet temperature within the 1180 °C to 1270 °C range is assumed. The overflow slag temperature is set to 1280 °C as the optimum value.

Figure 11 shows that the lowest slag input temperature of 1180 °C requires an energy input of about 4.5 MW to heat the slag to a target temperature of 1280 °C. As the slag input temperature rises to 1280 °C (equal to the output temperature), the required energy input decreases linearly to 1.5 MW. The analysis presented also shows that the average power consumption is 2.0 to 3.0 MW under expected operating conditions and can increase to 4.5 MW under extreme process conditions.

B. *Basic Design of Industrial MHD Slag-Cleaning Reactor*

For the industrial-type reactor design, the conventional reduction furnace (SAF) for slag cleaning has to be supplemented by an externally applied magnetic field (*via* electromagnet), which interacts with the electrode current to generate the Lorentz force and is responsible for the magnetohydrodynamic stirring effect. The reactor size for the industrial application and in particular the slag flow rate of 100 t/h is designed on the basis of an assume minimum slag residence time of 40 minutes, like the pilot plant in Hamburg. With the objective of an improved settling rate, the slag reactor volume is determined for an increased residence time of 60 minutes. As shown in analysis step (d) in Figure 2, the rectangular furnace concept is derived based on calculation principles for furnace dimensioning to existing, rectangular copper slag-cleaning furnaces (*e.g.*, Birla Copper, Frist Quantum, Kazzinc), as shown in Figure 12.

The cross-section shows two liquid layer, copper matte (0.25 m) and slag (1.0 m) on which a coke layer 0.2 m thick floats. The DC energy supply system, like the pilot furnaces, is also equipped with two anode electrodes plus the bottom cathode electrode, with most of the energy input *via* the front electrode. Both electrodes are immersed in the coke and slag.

The iterative industrial furnace design in analysis step (c) and step (d) in Figure 2 results in a required magnetic field strength of up to 20 Gauss. If one analyzes the simple, rectangular furnace, the fundamental question is how to generate a magnetic field of this intensity in the middle of an electromagnet gap of up to 5.5 m. In the literature available, there are no rules that allow the distribution of the magnetic field in gaps larger than 0.5 m to be determined.[24–28]

Drawing on the basic relationships from the field tests in Figures 7 and 8, the following magnet coil design is calculated for a pole area of 1600 cm^2 (40 × 40 cm) and two coils on each side for the different industrial furnace shapes. With a magnetic reluctance in the air gap between the poles of 250 cm (= reactor type 2), 350 cm (= reactor type 3) and 550 cm (= reactor type 4)

$$R_g = \frac{250/350/550}{(\mu_0 \cdot 1600)} = 1.647 \text{ to } 3.647 \cdot 10^7 \frac{\text{henry}}{m} \quad [9]$$

an air permeability distribution, μ_0, of

$$\mu_0 = 3 \cdot \pi \cdot 10^{-7} \frac{\text{henry}}{m} \quad [10]$$

and magnetic flux to the consisting pole area at 20 Gauss

$$Wb = 20 \cdot 1600 = 3.2 \cdot 10^{-4} \text{ weber} \quad [11]$$

the resulting ampere winding per coil is as follows:

$$\theta = R_g \cdot Wb \quad [12]$$

for reactor type 2 = 5305 A-turns; reactor type 3 = 7427 A-turns; and reactor type 4 = 11,671 A-turns.

Determining the optimal size and shape of the front reactor zone, the accurate magnetic field intensity and the parameters of the DC power source are the key elements here. To this end, the slag residence time and velocity are analyzed in the next section by means of CFD simulations and compared with the pilot-scale results (see analysis step (c) in Figure 2).

IV. COUPLED CFD SIMULATION

A. *Numerical Model*

The processes in the DC electric furnace are not steady; they are rather slow and can be described with a quasi-steady or simply steady formulation. In the numerical FLUENT model, equations for mass, momentum, and energy conservation are solved by means of the following governing equations. In addition to the continuity and Navier–Stokes equations, electromagnetic Maxwell's equations are solved in ANSYS to predict the electric current density and magnetic fields.

CFD simulations are simplified by making a number of assumptions regarding steady-state condi-tion, non-compressible flow, standard k-ε turbulence model for matte, and single-phase flow. The fluid flow equations in FLUENT are described using the continuity and Navier–Stokes equations:

$$\frac{\partial \rho}{\partial t} + \nabla \cdot (\rho \vec{v}) = 0 \quad [13]$$

This equation is valid for both compressible and incompressible flows. For incompressible fluids, the density ρ is constant and the continuity equation is:

$$\nabla \cdot \vec{v} = 0 \quad [14]$$

Core of the Navier–Stokes equations is the momentum conservation equation:

$$\rho \frac{\partial}{\partial t}(\rho \vec{v}) + \nabla(\rho \vec{v} \vec{v}) = -\nabla p + \nabla \cdot (\bar{\bar{\tau}}) + \rho \vec{g} + \vec{F} \quad [15]$$

Here, p represents static pressure, $\bar{\bar{\tau}}$ is the stress tensor, $\rho \vec{g}$ and $\vec{F}$ are the gravitational body force and external body forces respectively. The stress tensor $\bar{\bar{\tau}}$ is expressed as follows:

$$\bar{\bar{\tau}} = \mu \left[\left(\nabla \vec{v} + \vec{v}^T \right) - \frac{2}{3} \nabla \cdot \vec{v} I \right] \quad [16]$$

where μ is the molecular viscosity, and I is the unit tensor.

When temperature, pressure, and the fluid density (of slag and matte) remain constant along a trajectory (*i.e.* it is incompressible), a simplified momentum equation can be used[47]:

$$\frac{\partial \vec{v}}{\partial t} + (\vec{v} \cdot \nabla) \vec{v} = -\nabla p + \mu \Delta \vec{v} + \vec{F} \quad [17]$$

The user-defined volume force density $\vec{F}$ in terms of the unit volume is coupled in FLUENT with the Lorentz force (imported FMAG from ANSYS) and buoyancy force, due to natural convection.

Temperature-dependent density is used to study free convection (buoyancy force effects). Therefore, the pressure gradient in the momentum equation [15] is rewritten as:

$$\frac{\partial p}{\partial x} + \rho \vec{g} = > \frac{\partial p'}{\partial x} + (\rho - \rho_o) \vec{g} \qquad p' = p - \rho_o \cdot g \cdot x \quad [18]$$

The energy equation is expressed as follows:

$$\frac{\partial}{\partial t}(\rho E) + \nabla \cdot (\vec{v}(\rho E + p)) = \nabla \cdot \left(k_{eff} \nabla T - \sum_j h_j \vec{J}_j + (\bar{\bar{\tau}}_{eff} \cdot \vec{v}) \right) + S_h \quad [19]$$

where k_{eff} represents effective conductivity and $\vec{J}_j$ is the diffusion flux of species j. S_h represents the heat of chemical reactions and any other volumetric heat sources with the energy term

$$E = h - \frac{p}{\rho} + \frac{v^2}{2} \quad [20]$$

The incompressible flow is expressed as

$$h = \sum_j Y_j h_j + \frac{p}{\rho} \quad [21]$$

and the enthalpy for the mass fraction Y_j of species j is

$$h_j = \int_{T_{ref}}^{T} c_{p,j} dT \quad [22]$$

Because the FLUENT model for MDH slag cleaning does not include dissipation components and diffusion terms, energy equation [19] can be simplified as follows:

$$\frac{\partial}{\partial t}(\rho E) + \nabla \cdot (\vec{v}(\rho E + p)) = \nabla \cdot (k_{eff} \nabla T) + S_h \quad [23]$$

Table II. ANSYS Element Settings SOLID117

Element Type (KEYOPT)	Material Region	Degree of Freedom (DOF)	Formulation	Relevant Equation
117	Refractory	12 AZ	Magnetic only	[30]
117,1	Electrode, coke, magnet,	12 AZ and 8 VOLT	Eddy current, time integrated VOLT	[27], [28], [29], [30]
117,1,1	Slag, matte	12 AZ and 8 VOLT	Conventional velocity formulation	[27], [28], [29], [30], [31], [32]

The user-defined volumetric heat source S_h is coupled with the Joule heat density (imported JHEAT from ANSYS), generated by the electrical conduction losses.

Laminar flow conditions are assumed in the slag phase. Kharicha *et al.*[7] used the SAS-SST K-omega model to simulate tornados and cyclones driven by magneto-hydrodynamic forces; Kazak *et al.*[13] used the k-ε turbulence model to simulate the turbulent of vortex flows in DC electric arc furnace. Perez[28] compares the k-ε RNG model, the k-ε Realizable model and the k-ε SST model to simulate the applicability of Lorentz forces in a coloring forehearth of molten glass tanks.

As the strengths and weaknesses of the standard k-ε model have become known, improvements have been made to the model to enhance its performance. Standard k-ε model for small Reynolds numbers is applied for the copper matte phase with the assumption that the flow is fully turbulent, and the effects of molecular viscosity are negligible. The turbulence kinetic energy (k) and its dissipation rate (ε) are obtained using the following equations:

$$\frac{\partial}{\partial t}(\rho k)+\frac{\partial}{\partial x_i}(\rho k u_i)=\frac{\partial}{\partial x_j}\left[\left(\mu+\frac{\mu_t}{\sigma_k}\right)\frac{\partial k}{\partial x_j}\right]+G_k+G_{kb}-\rho\epsilon-Y_M+S_k \quad [24]$$

$$\frac{\partial}{\partial t}(\rho \epsilon)+\frac{\partial}{\partial x_i}(\rho \varepsilon u_i)=\frac{\partial}{\partial x_j}\left[\left(\mu+\frac{\mu_t}{\sigma_\varepsilon}\right)\frac{\partial \varepsilon}{\partial x_j}\right]+C_{1\varepsilon}\frac{\epsilon}{k}(G_k+C_{3\varepsilon}G_b)-C_{2\varepsilon}\rho\frac{\varepsilon^2}{k}+S_\varepsilon \quad [25]$$

where, G_k represents the generation of turbulence kinetic energy, G_b is the generation of turbulence kinetic energy *via* buoyancy and Y_M represents the contribution of the fluctuating dilatation. $C_{1\varepsilon}$, $C_{2\varepsilon}$ and $C_{3\varepsilon}$ are constants. In addition, σ_k and σ_ε are the turbulent Prandtl numbers for k and ε respectively. S_k and S_ε are user-defined source terms with a value of 0.6. After determining k and ε, the following equation is used to calculate the eddy viscosity (μ_t):

$$\mu_t=\rho C_\mu\frac{k^2}{\epsilon} \quad [26]$$

where C_μ is a constant. The model constants $C_{1\varepsilon}$, $C_{2\varepsilon}$, C_μ, σ_k and σ_ε have the following default values[47]: $C_{1\varepsilon}$, = 1.44, $C_{2\varepsilon}$ = 1.92, C_μ = 0.09, σ_k = 1.0, σ_ε = 1.3

The electromagnetic processes are governed by Maxwell's equations and solved in ANSYS. Four equations denote the electric field intensity, $\vec{E}$, the magnetic field intensity, $\vec{H}$, the electric flux density, $\vec{D}$, the magnetic flux density, $\vec{B}$, and the electric current density, $\vec{J}$[48,49]:

$$\nabla\times\vec{E}=-\frac{\partial B}{\partial t} \quad [27]$$

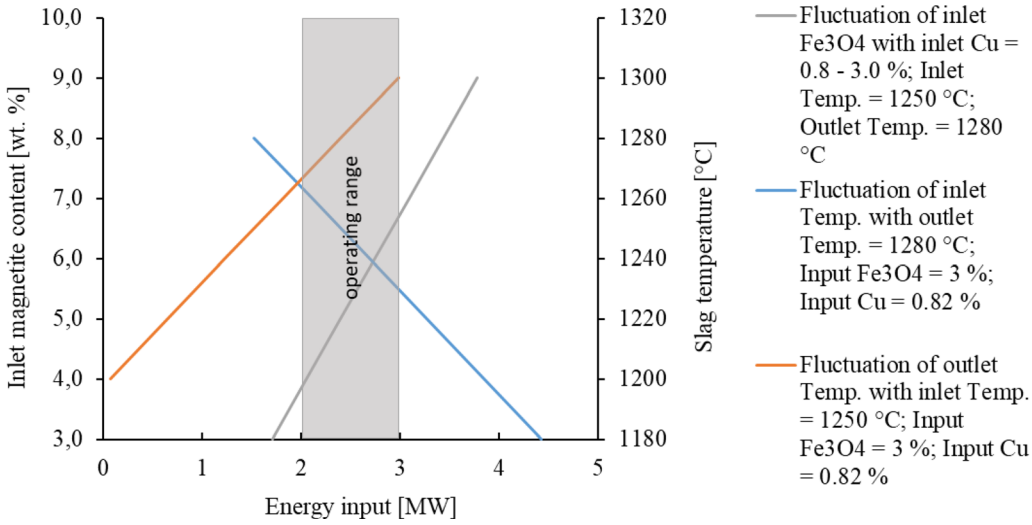

Fig. 11—Electrical energy input as a function of varied slag temperatures (input and output) and fluctuate magnetite contents.

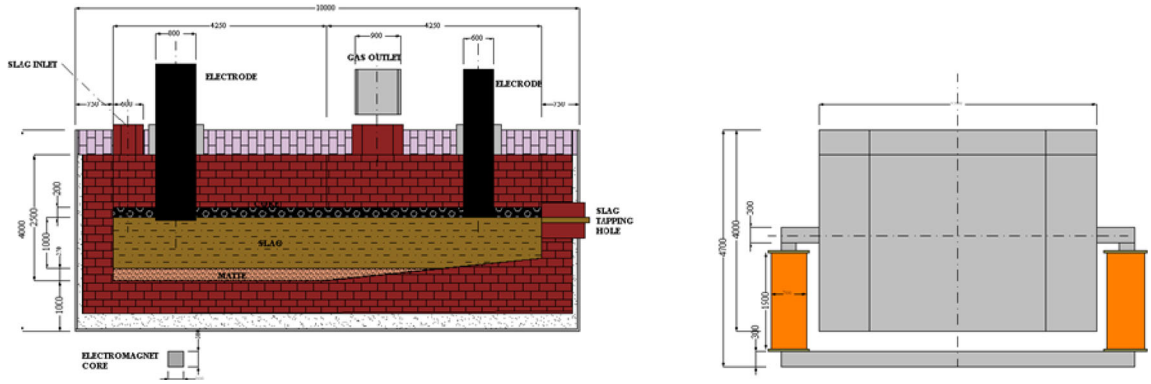

Fig. 12—100 t/h MHD rectangular industrial furnace concept (with hearth dimensions of 8.5 m × 4.0 m).

$$\nabla \times \vec{H} = \vec{J} \quad [28]$$

$$\nabla \times \vec{D} = \rho \quad [29]$$

$$\nabla \times \vec{B} = 0 \quad [30]$$

Ohm's law for fluid motion with specific conductance σ and liquid velocity $\vec{v}$ (imported from FLUENT) is

$$\vec{J} = \sigma(\vec{E} + \vec{v} \times \vec{B}) \quad [31]$$

and the Lorentz force $\vec{F}$, which the electromagnetic field exerts on moving electric charge q, is

$$\vec{F} = q(\vec{E} + \vec{v} \times \vec{B}) \quad [32]$$

For a proper electromagnetic analysis, the continuity equation must be satisfied and the source density must be solenoidal. This means that the current density must satisfy the law of conservation of matter.[50]

$$\nabla \cdot \vec{J} = 0 \quad [33]$$

In a harmonic analysis, any field quantity $q(r, t)$, which depends on the space r, and time, t, may be expressed as the real part of the complex function:

$$q(r,t) = Re\{Q(r)e^{j\omega t}\} \quad [34]$$

In the electromagnetic analysis, $q(r, t)$ can be the flux density, $\vec{B}$, the magnetic field, $\vec{H}$, the electric field, $\vec{E}$, the current density, $\vec{J}$, the vector potential, $\vec{A}$, or the scalar potential, V. The magnetic scalar potential cannot be used for current-carrying areas within electrical conductors.

For this purpose, a magnetic vector potential $\vec{A_z}$ (AZ in ANSYS) can be defined. The electrical potential φ used (VOLT in ANSYS) is then a time-integrated potential.[49]

Note, however, that $q(r, t)$ cannot be the Joule heat, Q^j, and the force density, F^{jb}, because they include a time constant term. The solution for harmonic analysis is described in the numerical coupling in Section IV–C below.

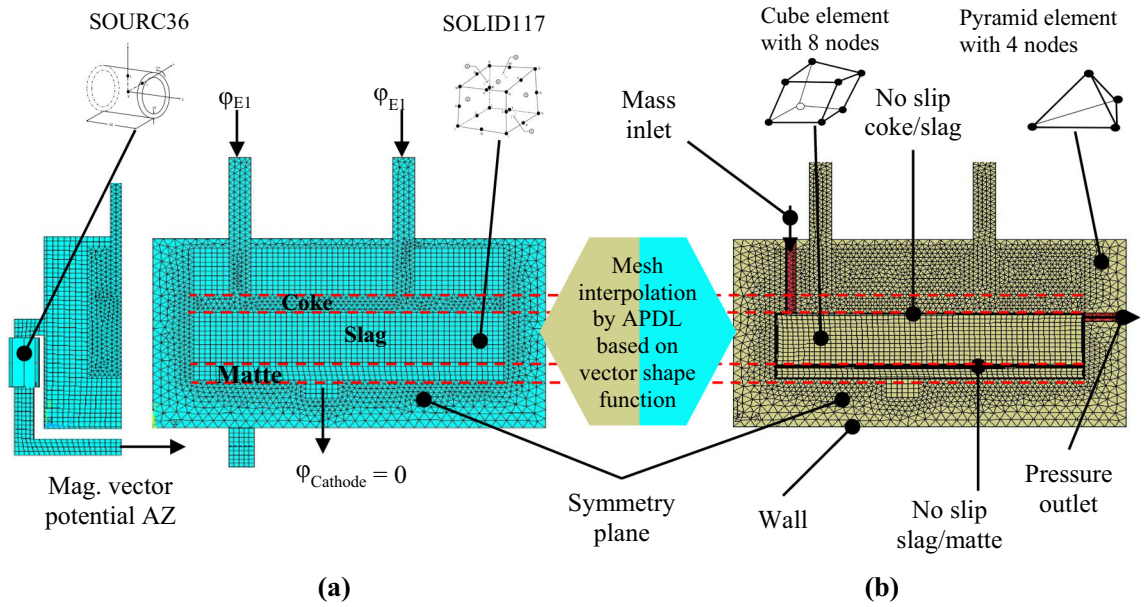

Fig. 13—Basic mesh models for the electromagnetic calculations in (*a*) ANSYS and the CFD calculations in (*b*) FLUENT with the corresponding boundary conditions.

B. *Geometry Modeling and Boundary Conditions*

The illustration in Figure 13 shows two basic mesh models for the electromagnetic calculations in ANSYS (a) and the CFD calculations in FLUENT (b) with the corresponding boundary conditions. The superordinate boundary conditions applied to the geometrical model are:

- No-slip condition on the liquid interface and reactor walls (velocity vector equal to zero).
- Pressure outlet on the surface of the outlet channel (pressure equal to zero).
- Slag temperature inlet distribution equal to the temperature measurements (cf. Figure 11).
- Slag mass flow inlet with an average throughput of 100 t/h on the entrance surface of the inlet channel.
- Electric potential of 96 to 180 V on the front anode electrode (electrode 1) corresponding to the required reactor power and of 0 V on the bottom cathode electrode.
- Ampere winding of up to 11,671 A-turns per magnet coil to ensure a magnetic flux density of up to 20 Gauss.
- Combined external convection and radiation boundary conditions at the outer reactor walls with constant thermal conductivity, k, and capacity, c_p, as well constant emissivity, ε_{ext}.

Due to the geometrical symmetry, and to save processing capacity, the numerical simulation is limited to one-half of the reactor. The resulting meshes consist of up to 2.5 million cells with different type of elements and is refined in FLUENT for the slag/refractory, slag/coke and slag/matte flow interfaces.

For all types of analysis on the axis of symmetry of the calculation domain, the following conditions apply:

$$\frac{\partial v}{\partial z} = 0, \frac{\partial k}{\partial z} = 0, \frac{\partial \varepsilon}{\partial z} = 0, \frac{\partial \varphi}{\partial z} = 0$$

For the simulation in FLUENT, structured hexahedral elements are used in the flow regions (slag and matte) and tetrahedral elements outside of these (*e.g.*, in the refractory). In contrast to unstructured grids, these are nearly symmetrical.

Preliminary studies have shown that the symmetry of the mesh is extremely important for the calculation of flow patterns, as asymmetric flows will otherwise result due to numerical diffusion.

The no-slip boundary condition is used for magnetohydrodynamic processes at all liquid boundaries, both on the boundary of the liquid slag with the coke, and the boundary of liquid matte with slag. The last approximation is based on the fact that slag viscosity is much higher than the liquid matte viscosity, and it can be considered as no-slip condition.

Sheng *et al.* already reported for his created CFD models that a non-slip boundary condition between the slag and the matte was required to achieve a good match between simulated and measured temperature profiles.[20] Hadley *et al.* even specified the matte zone as solid layer and only calculated the flow profiles in the slag.[23] However, this interface is, regarded as critical when the heat transfer from slag to matte is studied. Preliminary research shows that with added heat sinks in the slag and a turbulence model for the matte, the difference between the slag temperature and the matte at the non-slip boundary condition is resolved.[51] Mathematically, it means that velocity and turbulent components were all set to zero.

$$\vec{v} = 0, k = 0, \varepsilon = 0$$

Table III. Material Properties for the Coupled Numerical Simulation

Material	Density ρ kg/m^3	Viscosity μ Pa s	Electrical cond σ 1/Ω m	Thermal cond k W/m K	Thermal capacity c_p J/kg K
Slag	$\rho_S = 3500[1 - \beta_S(T - T_{1523})]$ with $\beta_S = 7 \cdot 10^{-5}$ 1/K	$\eta_S = 0.43e^{\frac{169}{T-1080}}$	80	2.0	1050
Matte	$\rho_M = 4900[1 - \beta_M(T - T_{1423})]$ with $\beta_M = 1 \cdot 10^{-6}$ 1/K	$\eta_M = 0.000336e^{\frac{5000}{T}}$	5000	5.5	1500
Coke	1000	—	50	20	1000
Refractory	3000	—	$1{\cdot}10^{-5}$	3.5	1200
Electrode	1700	—	15,000	20	2000

The energy equation is solved to determine the temperature T in the melt. The heat flux at the outer reactor wall is modeled as combined external heat transfer condition

$$\dot{Q} = h_{ext}(T_{ext} - T_w) + \epsilon_{ext}\sigma(T_\infty^4 - T_w^4) \qquad [35]$$

where h_{ext} represents external heat transfer coefficient, T_{ext} is the external heat-sink temperature; these are predefined. The Stefan-Boltzmann constant, σ, and emissivity, ε_{ext}, are constant. T_w is the surface temperature of the wall and T_∞ is equal to the ambient temperature.

In the ANSYS mesh, a part of the neighborhood is also mapped (not shown in Figure 13(b)) in order to take into account the magnetic field in the empty space. For the coupled calculation of electromagnetic fields in ANSYS, a block-structured hexahedral grid is used. With element SOLID117 consisting of 20 nodes, It has 12 edge-flux DOFs (Degree Of Freedom), one at each midside node. The eight corner nodes carry the time-integrated electric potential DOF or the electric potential. The electromagnetic properties in ANSYS are assigned to the different material regions *via* the following element options (KEYOPT):

By setting KEYOPT (2) = 1 for the slag and matte elements, the velocity effects in the liquids (imported from FLUENT) are activated as a moving conductor. 3D harmonic analysis with a moving conductor also requires that the moving conductor region include the time-integrated electric DOF (VOLT), therefore KEYOPT (1) = 1 (AZ, VOLT degrees of freedom).

ANSYS can calculate coupled 3D magnetic fields and the resulting electromagnetic force effects with Eq. [32]. The current flow of the coil, which generated the magnetic field, is defined as the volume current density in the area of the windings with the SOURCE36 element. The magnetic vector potential in the magnetic iron core is perpendicular to the symmetry plane (cf. Figure 13(a))

$$\frac{\partial A_z}{\partial x} = 0, \frac{\partial A_z}{\partial y} = 0$$

The material properties used in the models are taken from basic, laboratory-scale experiments (*e.g.*, slag and matte samples from slag-cleaning furnace) and are continuously matched to the simulations results across all pilot test series.[52] Table III summarizes the various material properties used for the numerical calculations in ANSYS and FLUENT.

The numerical calculations in FLUENT took into account the temperature dependence of the fluids (for slag and matte) for both density and viscosity. For an average thermal expansion coefficient of 1 kg m^{-3} K^{-1}, the slag density can be expressed as a function of the temperature, with a constant thermal expansion coefficient of $\beta_S = 7 \times 10^{-5}$ 1/K. Matte density is also given as a function of the temperature, with a thermal expansion coefficient of $\beta_M = 1 \times 10^{-6}$ 1/K.

The magnetic field calculation in ANSYS uses the saturation curve (B-H curve) in Figure 8(b) for the magnetic iron core (material: ferromagnetic soft iron) which was confirmed in the field test measurements. For the remaining materials, a relative magnetic permeability of $\mu_r \sim 1$ is assumed because of their paramagnetic material properties.

C. *Coupled Numerical Setup*

As shown in the analysis step (c) in Figure 2, a coupled CFD model is set up to represent the electromagnetic conditions for the reactor design, which together with the pilot test results enabled conclusions to be drawn about reaction kinetics and copper recovery for mass and energy balance.

A numerical coupling between the two meshes in the flow region has to be performed, and the relevant results interpolated to the opposite mesh (node points). For this purpose, ANSYS provides an APDL (Ansys Parametric Design Language) interpolation file based on the finite element method. Simple function is used to describe the vector potential $\vec{A}$ inside each finite element with the vector shape function w_i used to determine the placement function α_i and edge direction $\vec{q}_i$[53]:

$$\vec{A}(x, y, z) = \sum_{i=1}^{12} w_i(\vec{r})A_i \qquad [36]$$

$$w_i(\vec{r}) = \alpha_i(u, v, p)\vec{q}_i(\vec{r}) \qquad [37]$$

using:

$$\vec{r}(x, y, z) = \hat{i}x + \hat{j}y + \hat{k}z \qquad [38]$$

Initially, the distribution of the electric current density and the magnetic flux density are computed using Eqs. [27] through [33]. As described in the previous Section IV–B, ANSYS element SOLID117 considers

convection and can be used to represent the influence of moving slag on the magnetic field. Disadvantage is that the elements can only calculate convection (flow) harmonic. The harmonic complex electromagnetic function (34) describes the steady state reached when a system is excited sinusoidally. The physical, time-varying field for a variable, $q(r, t)$, such as B, H, E, J, the vector potential or the scalar potential, which depends on space, r, and time, t, can be simplified:

$$q(r,t) = c(r)\cos(\omega t) - s(r)\sin(\omega t) \quad [39]$$

where $c(r)$ and $s(r)$ are the real and imaginary parts of the complex function and ω is the angular frequency. Phase reference is established in such a way that the magnitude of the real solution describes the measurable field at $\omega t = 0$, whilst the magnitude of the imaginary solution describes the measurable field at $\omega t = -90$ deg.[48]

Therefore, it must be assumed that the AC current is temporally weak despite stationary conditions. However, the frequency of the electric current is so low ($f = 0.001$ Hz) that temporal fluctuations have no influence on the electromagnetic fields and force effect. For the electric field, the real component corresponds to the electric current density and the imaginary component to the electric potential. To calculate the current–voltage distribution, the time-integrated electric potential must be multiplied by the angular frequency (or angular velocity).

It should be noted that the Joule power density (output as JHEAT in ANSYS) and the electromagnetic force density (output as FMAG in ANSYS) are not subject to this periodic function. For the Joule power density Q^j and the force density F^{jb} an average force or power over a defined time unit is calculated[48]:

$$F^{jb} = 1/2(J_r B_r + J_i B_i) \quad [40]$$

$$Q^j = 1/2(J_r E_r + J_i E_i) \quad [41]$$

To determine the real value at time $t = 0$, the Joule heat or the magnetic force density has to be multiplied by two. The imaginary part at this time is zero. The element force is distributed among nodes to prepare a magneto-structural coupling. The average Joule heat can be directly applied to thermoelectric coupling. ANSYS writes results from an edge-based harmonic magnetic analysis to the magnetics results file, for the following derived data:

- Nodal Lorentz magnetic forces (FMAG; components X, Y, Z, SUM)
- Joule heat rate per unit volume (JHEAT)

The Lorentz force density vector (F_x, F_y, F_z) and Joule heat rate per unit volume for the slag and matte elements are interpolated with the APDL file to the position of the FLUENT nodes and are considered as source terms of the momentum [17] and energy Eq. [23]. In FLUENT, the user-defined volume force density $\overrightarrow{F}$ in terms of the unit volume is coupled with FMAG, and the user-defined volumetric heat source S_h is coupled with JHEAT.

Next, the momentum equation is solved to determine the velocity distribution and calculate the influence of the electromagnetic fields on the slag in FLUENT. A sequential solver (Pressure Based Solver) with implicit linearization is used to simulate the flow distribution in the slag and matte. The interpolation methodology adopted is the "Least-Squares Cell-Based" method, which is well suited to multiform meshes. For the single-phase steady-state CFD flow, a Second-Order-Upwind discretizes the continuity equation. In this approach, higher-order accuracy is achieved at cell faces through a Taylor series expansion of the cell-centered solution about the cell centroid. Thus when second-order upwinding is selected, the face value is computed using the following expression:

$$\phi_{f,SOU} = \phi + \nabla\phi \cdot \overrightarrow{r} \quad [42]$$

where ϕ and $\nabla\phi$ are the cell-centered value and its gradient in the upstream cell, and $\overrightarrow{r}$ is the displacement vector from the upstream cell centroid to the face centroid. With this formulation, the gradient in each cell has to be determined. The convective terms $(\overrightarrow{v}(\rho E + p)$ of the energy conservation equation are also discretized using a Second-Order-Upwind scheme. The pressure correction is performed with PISO (Pressure-Implicit with Splitting of Operators). To increase numerical stability, the PRESTO scheme is used for pressure discretization. Standard turbulence k–ε model for small Reynolds numbers is applied for the copper matte phase with Eqs. [24] and [25]. Laminar flow conditions are assumed in the slag phase. Due to the complexity of the numerical calculations (buoyancy effects and Lorentz forces), the numerical instability and the coupling of velocity, temperature and density (buoyancy), calculations must be carried out in an unsteady state.

Numerical back-coupling between the flow field in FLUENT and the electromagnetic field in ANSYS is considered to take into account real feedback effects. These effects occur when the change in the slag flow has a significant, *i.e.*, amplifying effect on other strongly temperature-dependent properties (*e.g.*, dynamic viscosity and density), which leads to a new change in the flow conditions. The numerical calculations show that the feedback effect in the industrial reactor is negligible due to the low flow velocities in the MHD zone and the large volume compared to the pilot reactor. Therefore, the interpolation loop *via* the APDL file is executed manually until the single result converges—on average a maximum of three loops are required—as shown schematically in Figure 14. The results of the individual numerical calculations are interpolated to the opposite geometry.

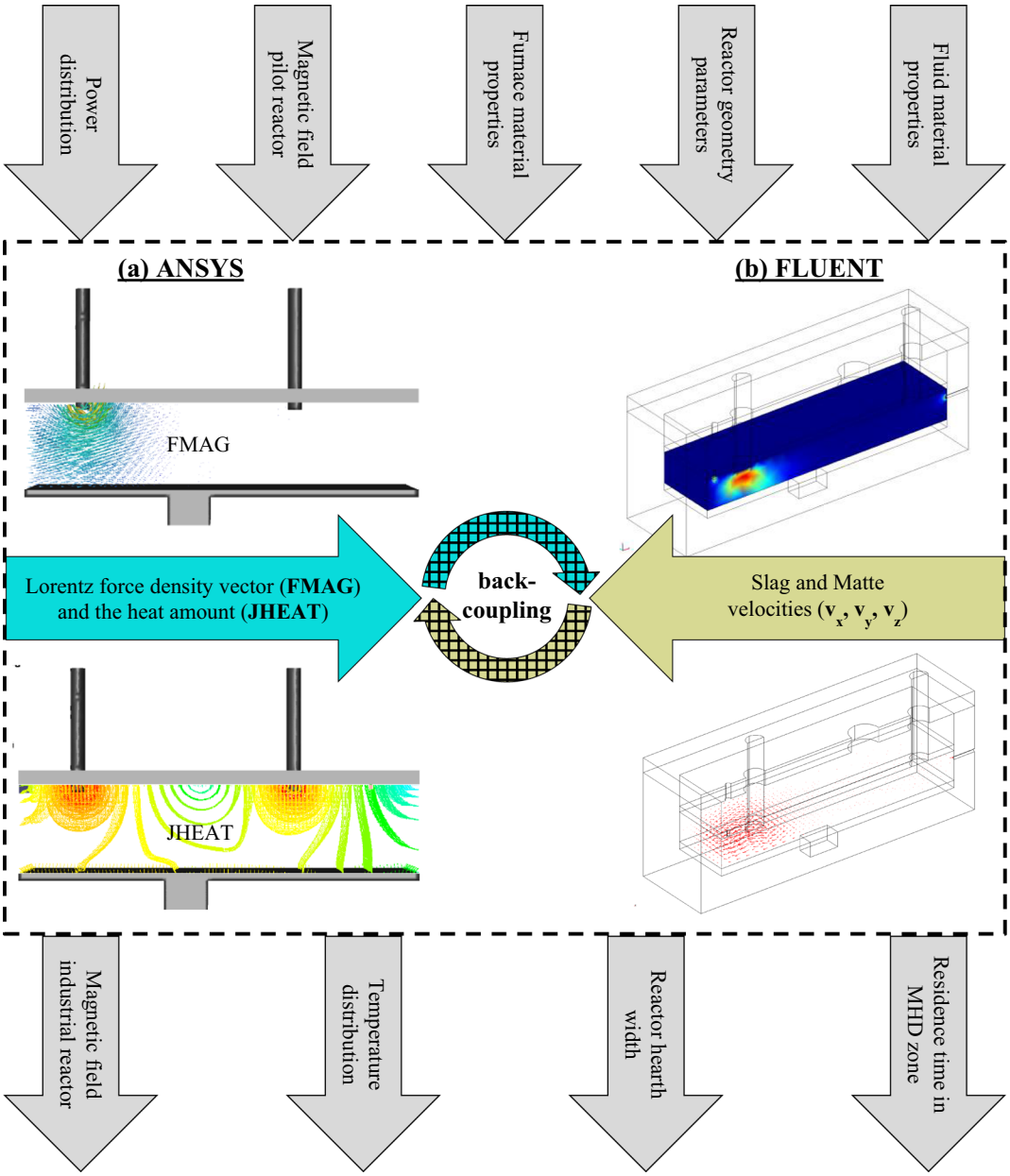

Fig. 14—Illustration: coupling of magnetic field (*a*) and flow (*b*) simulation with relevant outer information and resulting results.

An entire back-coupling loop is completed when the velocities (v_x, v_y, v_z) in slag and matte phase are solved using momentum conservation Eq. [17] and exported to ANSYS mesh for a new electromagnetic calculation. To write data that can be imported for post-processing, the FLUENT Export panel is used.

New harmonic electromagnetic analysis is subsequently started in ANSYS with the new liquid velocities (from FLUENT) for Ohm's law for fluid motion (31) and the Lorentz force on the moving electric charge [32]. In ANSYS, direct and iterative methods are available for solving the Maxwell's equations. In the default setting, the program is left to decide which solution algorithm is used. Edge formulation analyses can use the frontal solver (default), the sparse direct solver (SPARSE), the Jacobi Conjugate Gradient (JCG) solver, or the Incomplete Cholesky Conjugate Gradient (ICCG) solver. The frontal and ICCG solvers are recommended for harmonic edge analysis[50]—both are used for the presented simulation results in ANSYS.

V. RESULTS AND DISCUSSION

A. *MHD Simulation Results*

Numerical simulation using the finite element method (FEM) is a tool for investigating of electromagnetically generated flows. The major advantage of numerical calculations is that parameters can be freely varied and

in post-processing (post-processing of data and simulation display), for example, the flow lines can be displayed spatially as desired.

Aurubis AG in Hamburg results show better copper recovery from the slag at a lower magnetic field inductance (see Table I]. Repolarizing the magnetic field with a coil current of 16 A and pulsating clocking achieves the best copper recovery. In terms of power distribution between the electrodes, the 100:0 or 90:0 ratio has proven successful, highlighting the challenge of avoiding buildups in the discharge slag area (electrode 2). Concerning the settling behavior of the coagulated copper inclusions, a residence time of fewer than 30 minutes is evidence of deterioration.

Simulation results demonstrate that the deterioration of the copper settling behavior is caused by an intensive MHD rotational flow of slag and copper matte, which leads to the emulsification of the copper matte phase in the slag. At the boundary layer between the low-viscosity matte phase and the high-viscosity slag layer, the flow takes up a liquid copper film and disperses it into the slag. Another factor in the reduction of copper separation from slag is the partial reduction of the reactor volume of the pilot plants, caused by a narrow channel (with a reactor width of only 600 mm) and a reduced settling area. This results in a reduction of the residence time and coagulation of copper inclusions.

Based on these insights, the reactor shape and size of the industrial MHD slag-cleaning system in connection with magnetohydrodynamic stirring effects play a central role. These ultimately determined the slag residence time as well as the reaction rate and the MDH pattern of slag stirring in the front reactor section.

Three rectangular furnace shapes with different hearth widths based on the pilot furnace in Hamburg are analyzed and compared by calculating electrode current, voltage and delivered power in ANSYS. Flow profiles are created in FLUENT for different magnetic field intensities and used for further evaluation. The industrial scales (reactor types 2, 3, 4) are then compared with the pilot reactor from Hamburg (reactor type 1) to derive the optimal configuration. An overview of the main CFD result plots for the electric potential, velocity, and MDH flow distribution are shown in Figures 15, 16 and 18, with the corresponding details in sub-figures (a) through (e).

For the pilot reactor in Figure 15 (reactor type 1), a continuous slag throughput of 6 t/h is assumed, corresponding to a typical charging cycle in Hamburg of 2 t of slag added to the reactor within 20 minutes. During this time, the slag residence time in the reactor is 35 minutes, including 13 minutes in the MHD stirring zone.

Figure 15(b) with the electric current density and Figure 15(c) with the magnetic flux density and resulting Lorentz force illustrate the MDH effect for the slag cleaning reactor. The Lorentz volume force field on the fluid (slag) reaches its maximum all analyses under electrode 1, where the cross product of electric current density and magnetic flux density is concentrated. Due to the fixed electrode arrangement (anode to cathode), the flow topology (MHD rotation) is always directly linked to the magnetic flux density and results in the flow direction (cf. Figure 15(e)).

As already described, the lowest copper content in the overflow slag occurs at a lower magnetic field inductance, equivalent to a magnetic flux density of approx. 50 Gauss in the reactor center under the front electrode. As shown in Figure 15(d), at this magnetic field intensity the slag rotates under the electrode at a maximum velocity of 0.35 m/s at a current strength of 3 kA. A change in the magnetic field polarity leads to a change in the direction of the slag rotation (cf. Figure 15(e)). Increasing the magnetic field intensity to 100 Gauss increases the maximum velocity to 0.7 m/s below the electrode and 0.4 m/s at the slag-matte interface. In this case, the MHD rotation pattern is the same as the flow profile with 50 Gauss. However, Hamburg's results showed a decrease in copper separation at these higher strength fields.

Thus it can be concluded that the optimum magnetic field intensity is within the 50 Gauss range, and—for further investigations of the concept's industrial application—the maximum slag velocity should not exceed 0.5 m/s.

A comparison of the three industrial furnace shape concepts with a slag throughput of 100 t/h in Figure 16 (reactor type 2 and 3 with narrow MHD zone) and Figure 18 (reactor type 4 in initial furnace shape) gives an impression of the MHD slag transport through the reactor and the magnetic flux density required for this. Based on refractory wear observations at the pilot furnace in Hamburg, a decision was made in favor of a conventional rectangular furnace shape without a reduced inlet cross section (reactor type 4).

The first industrial applications (reactor types 2 and 3) to be investigated in Figure 16 with a slag throughput of 100 t/h are based on the pilot reactor (type 1) for the front MHD zone (with 1 and 2 m hearth width). The downstream settling and slag discharge zone (4 m width) is equal to the reactor width shown in Figure 12. With a magnetic field intensity of only 10 Gauss (at 2653 A-turns and 3714 A-turns) in Figure 16(b) and a required electrode current of 20 kA, a velocity of 0.35 m/s is generated under the electrode (cf. Figure 16(c)). This current supply results in a power input of about 3.6 MW to compensate for furnace heat losses and ensure the energy for relevant endothermic reactions and the target slag temperature. Increasing the magnetic field intensity to 50 and 100 Gauss raises the slag velocity to 1.8 and 3.6 m/s, respectively. In addition, the slag residence time in the MHD mixing zone is only 8 minutes, which rules out copper particle coagulation.

This also counteracts the emulsification of the copper matte phase into the slag phase. At the boundary layer from low-viscosity matte phase (η_M = 0.0089 Pa s at 1250 °C) to the overlying, high-viscosity slag layer (η_S = 0.59 Pa s at 1320 °C), the slag takes up a liquid matte film and disperses it back into the slag.

(a) φ_{E1} (electric potential) = U = 96 Volt

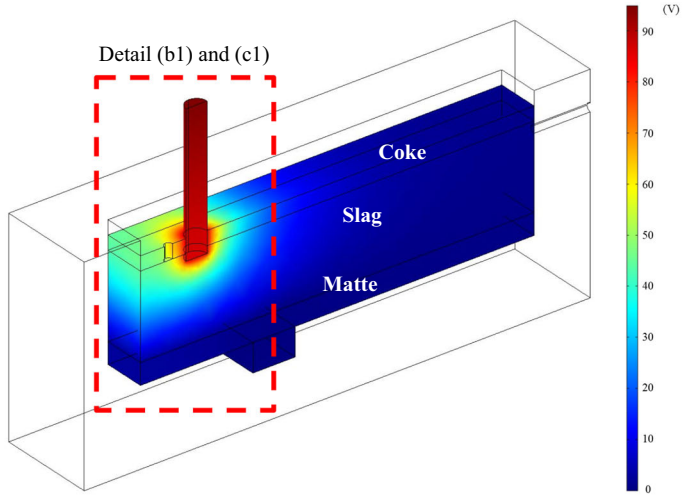

(b1) J (electric current density) with I = 3 kA **(b2)** Detail current density under electrode 1

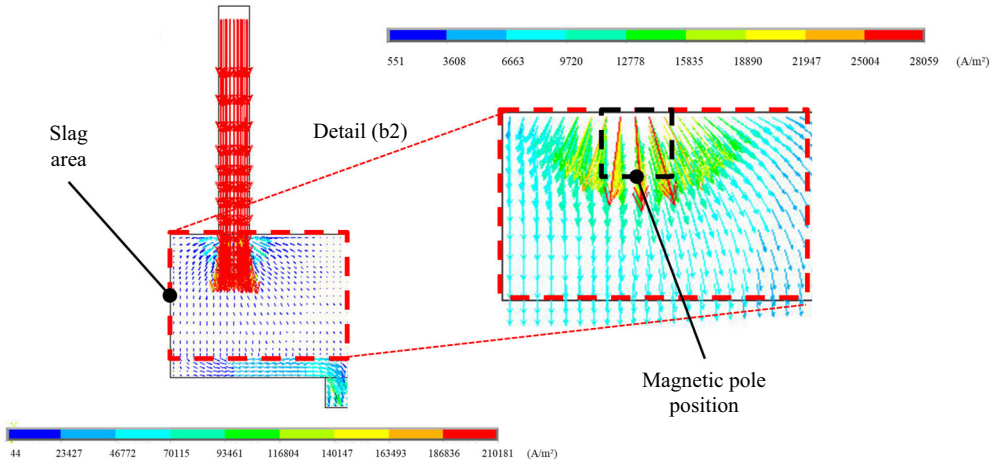

(c1) B_{gap} (magnetic flux density) = 50 Gauss **(c2)** FMAG (Lorentz force)

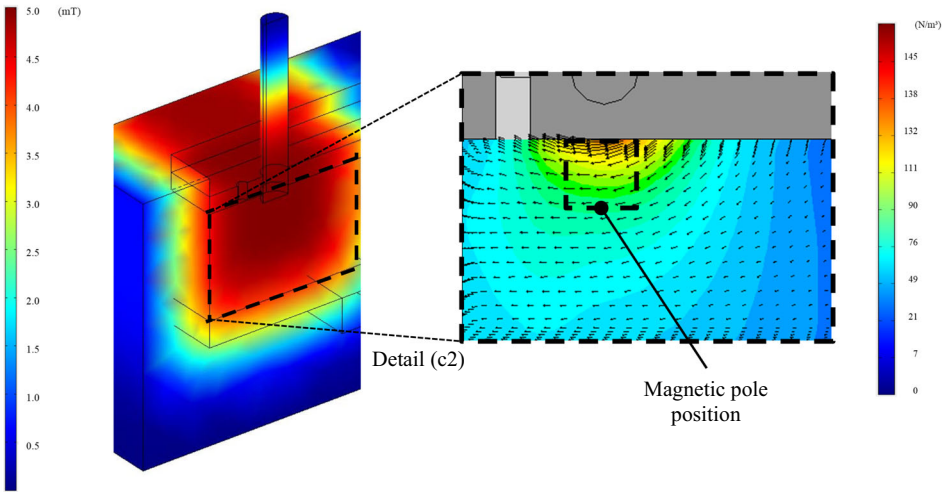

Fig. 15—Reactor type 1, pilot reactor in Hamburg with slag throughput of 6 t/h at B_{gap} = 50 Gauss and I = 3kA: (*a*) electric potential; (*b1*/*b2*) electric current density; (*c1*) magnetic flux density and (*c2*) Lorentz force; (*d*) velocity distribution; (*e1*/*e2*) MHD rotation pattern in slag area.

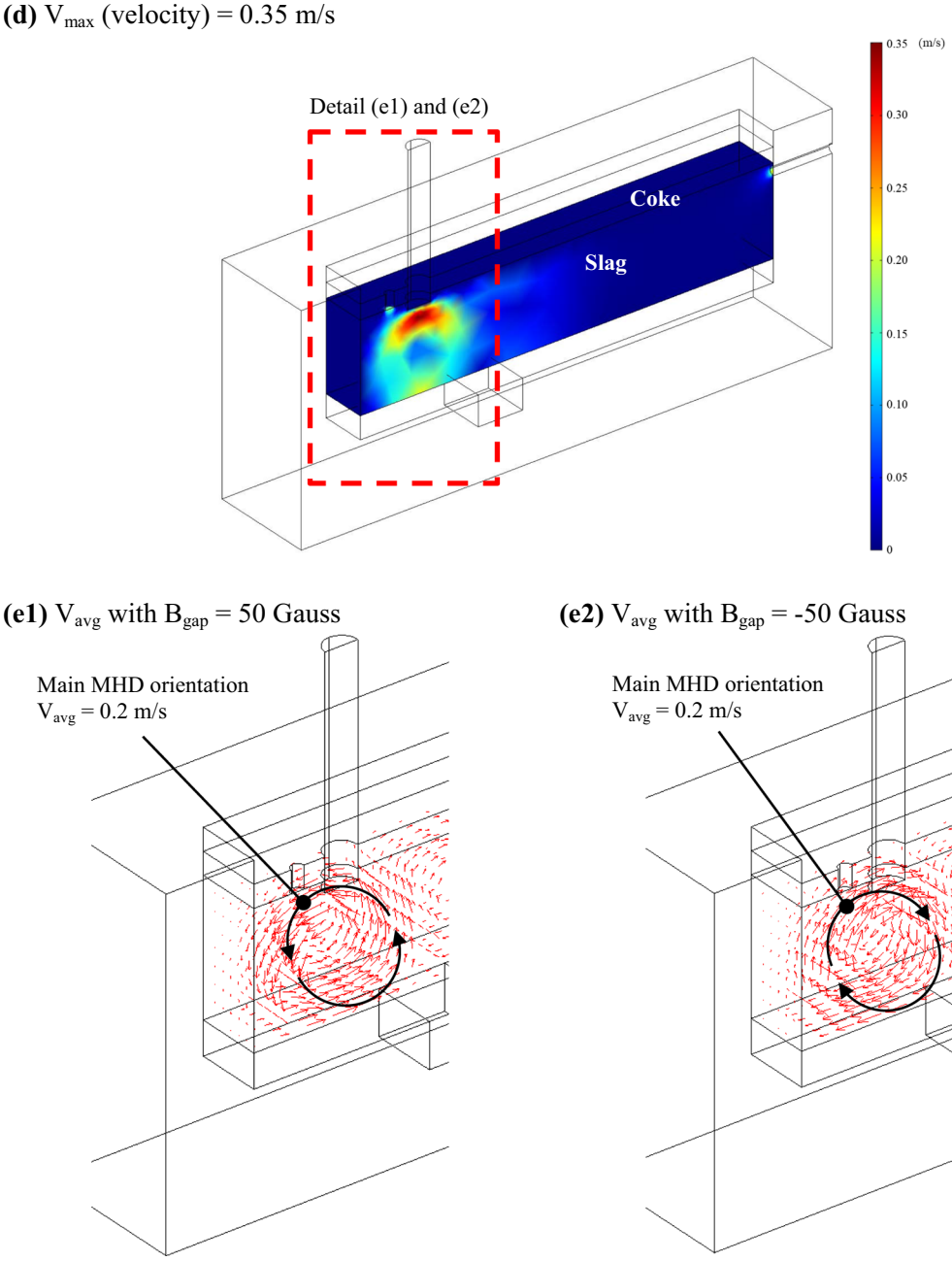

Fig. 15—continued.

The electrical energy in Figure 16(a) supplied *via* the electrodes generates up to 80 pct of the Joule heat at the contact surface between electrode and slag. Hot slag phase forms in the upper part of the reactor and colder phase in the lower part, interrupting natural convection. The MHD slag stirring counteracts and accelerates the exchange of oxides at the coke surface and thus the slag reduction rate assumed for the mass balance in Section III–A.

Comparing the MHD slag rotation in the pilot furnace in Figure 15(e), where the circulation is close to the ideal circle, with the slag rotation in the industrial furnace type 2 and 3 (Figure 16(d)), an elliptical slag movement with a lower velocity profile towards the copper phase is observed. It is more clearly visible in Figure 17 for reactor type 3, where the slag motion is partly horizontal. The differences are stronger for the same furnace at B_{gap} = -100 Gauss. Maximum slag velocity under the electrode 1 is 3.8 m/s and 1.0 m/s at matte interface.

Enlarging the MHD zone in the industrial reactor scale compared to the initial size described in Figure 12, with a uniform hearth width of 4 m, also promotes a significant change in the steady-state MHD flow situation. Changing the overall shape of the furnace to a conventional rectangular slag-cleaning furnace with outer dimensions of 10 m × 5.5 m creates a correspondingly large air gap for the electromagnet and increases

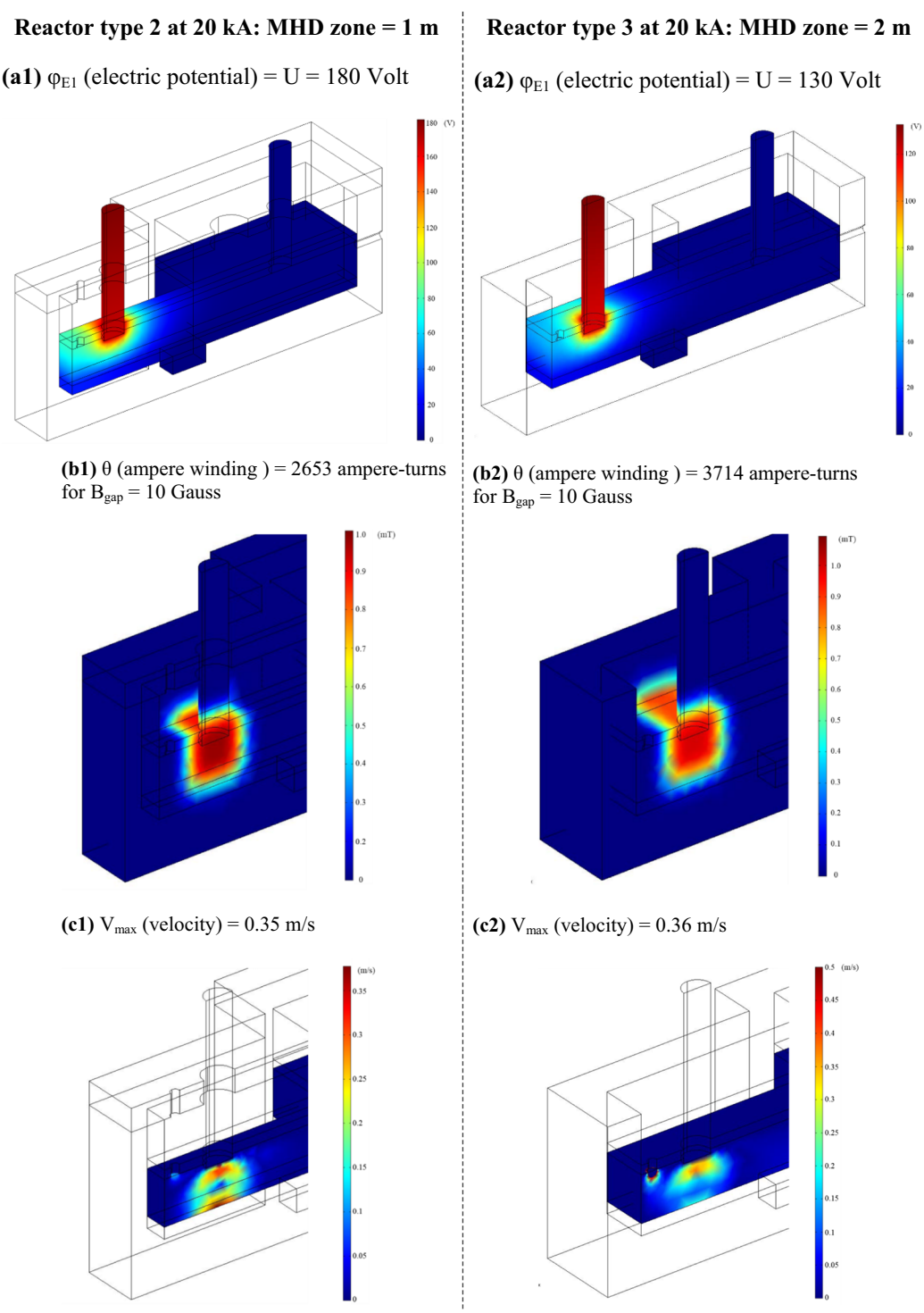

Fig. 16—Reactor type 2 and 3, industrial reactors with narrow MHD zone (1 m and 2 m) with slag throughput of 100 t/h at B_{gap} = 10 Gauss and I = 20 kA: (*a1*/*a2*) electric potential; (*b1*/*b2*) magnetic flux density; (*c1*/*c2*) velocity distribution; (*d1*/*d2*) MHD rotation pattern in slag area.

the ampere winding per coil up to 11,671 A-turns. In addition, the secondary voltage drops for the same electrode current intensity due to the change in the current density in the slag phase. As shown in Figure 18(a), under reactor type 4, the current intensity has to be increased to 26 kA to release a required power input of approx. 3 MW. Due to the fixed electrode arrangement (anode to cathode), the current distribution through the slag and matte is equal to the pilot reactor (type 1) in Figure 15(b)—again not shown here.

The magnetic field also expands hemispherically in the reactor (slag, coke and matte), as in all other analyses (cf. Figure 9), and the resulting Lorentz volume force on the slag reaches its maximum under the electrode, where

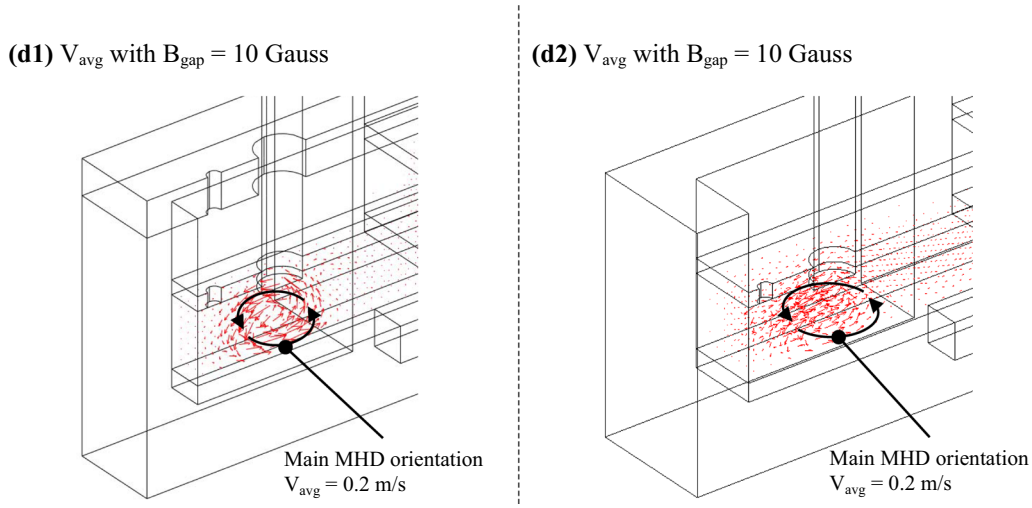

Fig. 16—continued.

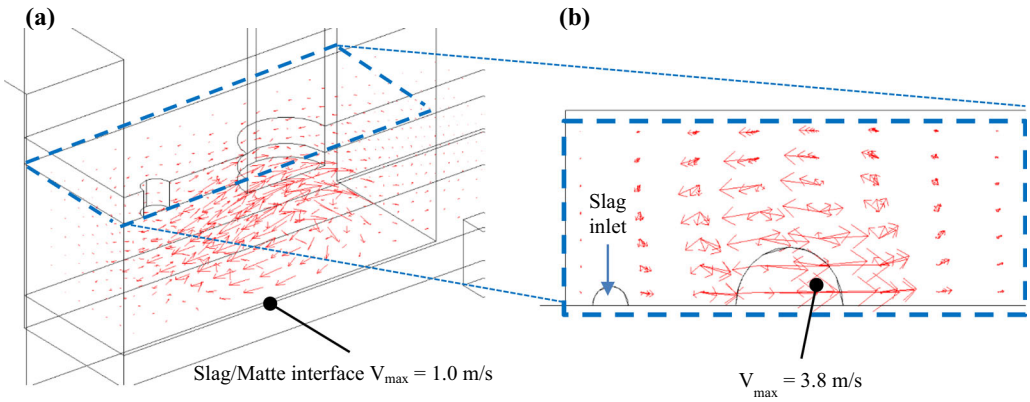

Fig. 17—Reactor type 3 with slag throughput of 100 t/h at B_{gap} = -100 Gauss and I = 20 kA: MHD rotation pattern in (*a*) slag area and (*b*) under electrode 1.

the cross product of electric current density and magnetic flux density is concentrated. The maximum slag velocity under the electrode at a magnetic flux density of 10 Gauss (with 5836 A-turns) is 0.5 m/s and 0.2 m/s near the slag-matte boundary layer. Due to the higher electrode current and the self-magnetic field generated, natural Lorentz forces now also dominate. These natural Lorentz forces are perpendicular to the electrode current and are proportional to it. Two MHD flow profiles are formed under the electrode with vertical and horizontal slag circulation with relatively high velocity. Figure 19(a) shows the slag circulation (due to the electrode current) under the same conditions with a magnetic flux density of only 20 Gauss (with 11,671 A-turns). The resulting maximum slag velocity is 1 m/s—and 0.4 m/s at the boundary layer to the copper matte phase. Figure 19(b) shows the vertical component of the slag movement under the electrode.

Changing electromagnet polarity (to $B = -20$ Gauss) results in MHD slag rotation with identical velocity and flow profile, but in the opposite direction as Figure 18(c). This meant that at 20 Gauss in the reactor core and with the appropriate electrode current intensity ($I > 10$ kA), the required slag velocity is easily achieved in a conventional rectangular slag-cleaning furnace.

For the preferred industrial application of reactor type 4, Figure 20 shows the maximum slag velocity as a function of the power input for a magnetic field inductance at 10 and 20 Gauss. For the determined average power input of 2.0 to 3.0 MW for a slag throughput of 100 t/h, the maximum slag velocity is expected within the 55 to 130 cm/s range.

The generated MDH slag flow pattern, as shown in Figure 19, in a vertical and horizontal orientation at higher electrode currents ($I > 20$ kA), enables optimal reactor volume utilization and eliminates stagnant liquid zones in the upper part of the reactor (which slows down

(a) φ_{EI} (electric potential) = U = 110 Volt

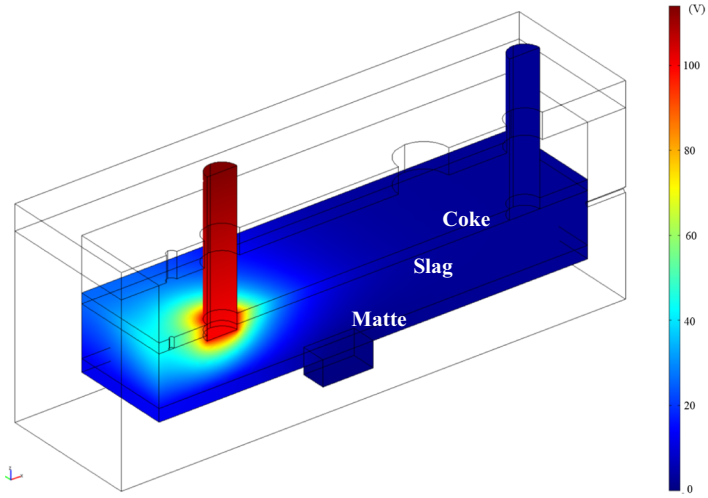

(b) V_{max} (velocity) = 0.5 m/s

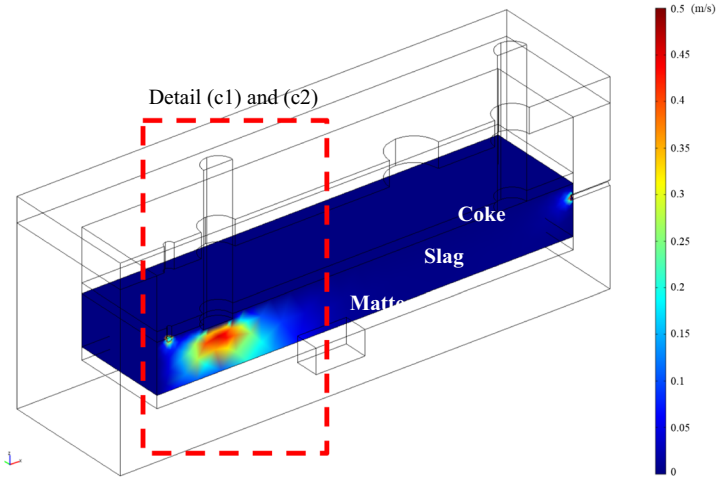

(c1) V_{avg} with B_{gap} = 10 Gauss

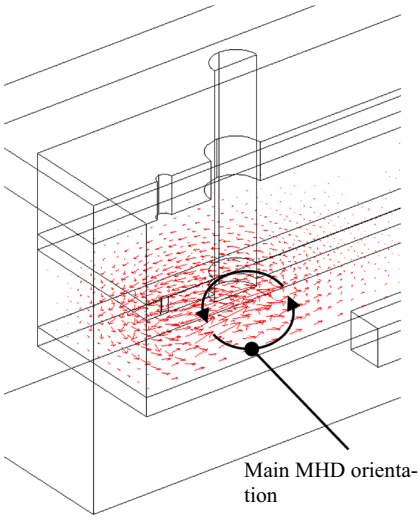

(c2) V_{avg} with B_{gap} = -10 Gauss

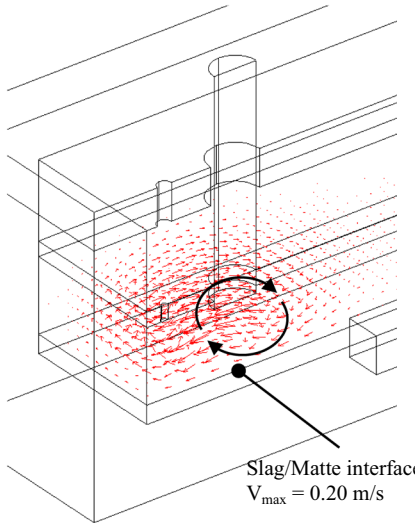

Fig. 18—Reactor type 4, industrial reactor in the initial shape (hearth width 4 m) with slag throughput of 100 t/h at B_{gap} = 10 Gauss and I = 26 kA: (*a*) electric potential; (*b*) velocity distribution; (*c1*/*c2*) MHD rotation pattern in slag area.

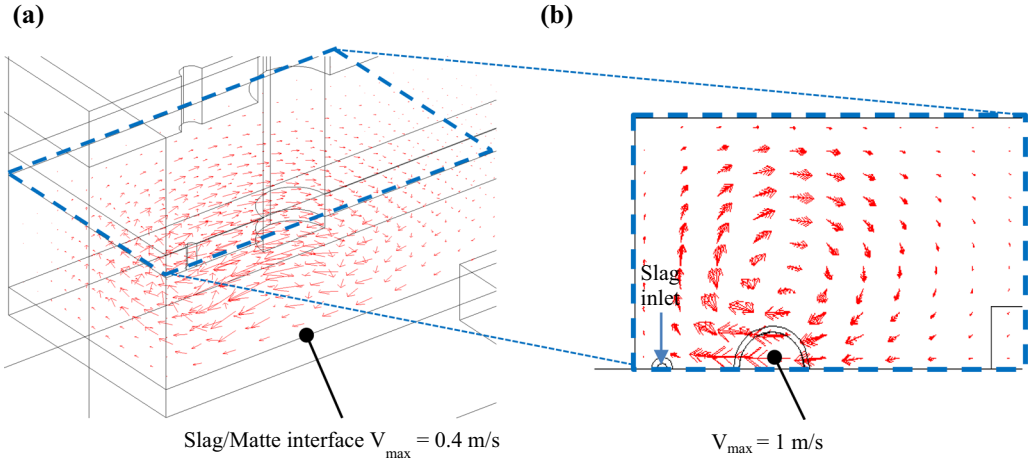

Fig. 19—Reactor type 4 with slag throughput of 100 t/h at B_{gap} = 20 Gauss and I = 26 kA: MHD slag rotation pattern in (*a*) in slag area and (*b*) under electrode 1.

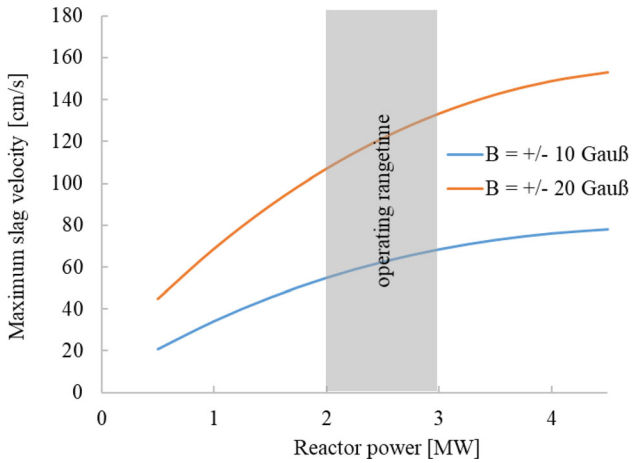

Fig. 20—Maximum slag velocity [cm/s] as a function of the reactor power [MW] for industrial furnace type 4 at magnetic flux densities of 10 and 20 Gauss (Slag properties: Throughput = 100 t/h; Inlet temp. = 1250 °C; Outlet temp. = 1280 °C; Magnetite content = 3 pct).

the mass and heat transport and reduces the degree of reduction of magnetite and copper oxides with the overlying coke).

B. *Implications for Industrial Furnace*

The industrial plant, like the pilot furnaces, is also equipped with two electrodes plus the bottom electrode, with most of the energy input *via* front electrode 1. The primary energy supply allows for a flexible energy input *via* both electrodes if a higher input *via* rear electrode 2 is required in the event of extended holding times as well as to avoid buildups in the run-out area. The flexible energy input control is linked to the constant slag tap temperature control, based on the process technology results from Hamburg. Continuous temperature measurements of the incoming and outgoing slag using high-temperature cameras are envisaged for this purpose.

The CFD simulation results show a required magnetic flux density of up to 20 Gauss in middle of a 5.5 m air gap in the reactor center. The design calculation, based on the collected field tests and simulation results require 11,671 A-turns per magnet coil. The industrial electromagnet has a U-shaped design with air-cooled coils and variable power control, like the pilot plant in Hamburg. The core is made from typical transformer plates in the form of 400 mm × 400 mm blocks. Two coils are made on square, fiber plastic boxes. Each coil has three layers of wire with a diameter of 3.05 mm, which for a maximum coil current of 20 A corresponds to 584 number of turns.

The industrial MHD slag-cleaning reactor is designed for continuous operation, which includes continuous or semi-continuous slag tapping. The mass and energy balances for different operating cases show that the average power consumption is 2.0 to 3.0 MW under the expected conditions, rising to 4 MW under extreme process conditions. The corresponding overview of the individual mass and energy flows is shown in Figure 21 for a slag throughput of 100 t/h.

The electric loss of approx. 0.35 MW is the sum of the ohmic loss resistances of the transformers, the high-current lines and the electrodes. However, this power loss can be influenced both positively and negatively by controlling the electric resistance of the slag bath (*e.g.*, by the electrode immersion depth). The inductive power loss is negligible because the reactor is operated with DC power.

A closed reactor operation is planned, *i.e.* the non-combusted off-gas has to be subsequently be post-combusted outside the reactor. This post-combustion should ideally take place with heat recovery by means of a waste heat boiler in order to utilize the energy heat of up to 0.5 MW.

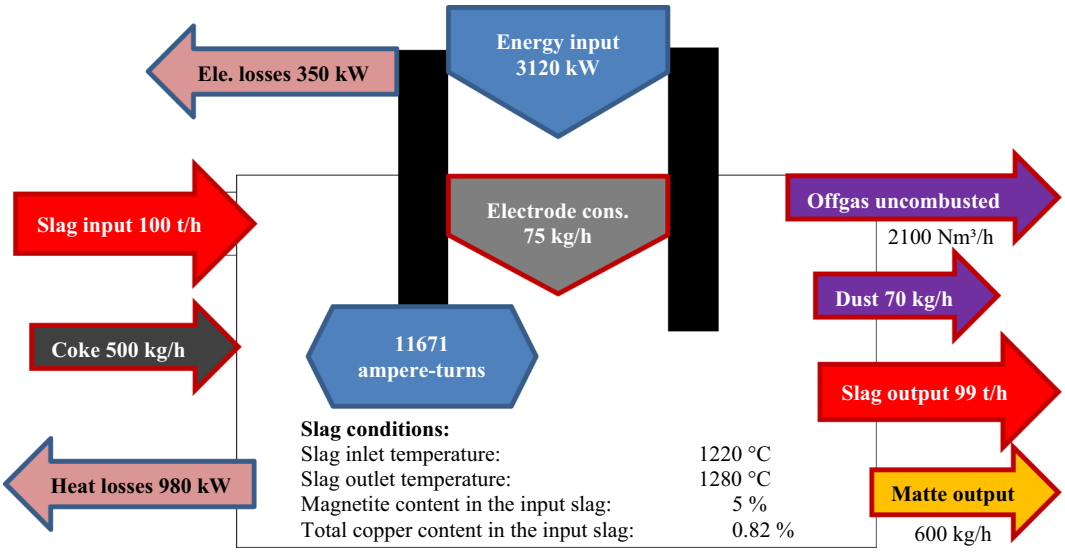

Fig. 21—Mass and energy flow diagram for MDH copper slag cleaning of 100 t/h; red arrow border = mass flows, blue arrow border = energy flows (Color figure online).

In terms of arrangement, the position of the tapping holes for the overflow slag and the accumulating copper matte corresponds to that of the pilot reactor in Hamburg. Therefore, the copper matte is tapped discontinuously and according to the degree of copper recovery. A significant component change compared to the pilot plants is the design of the bottom electrode; in Hamburg and Chile, a special form of the bottom electrode was implemented. From a coal block in the furnace bottom, a graphite electrode was fed upwards at the side of the furnace through the sidewall lining parallel to the upper electrodes and connected there to the energy supply by means of a contact shoe. This represented a simple solution. For industrial application, the "classic" SMS group bottom electrode is used *via* contact points in the furnace bottom to avoid oxidation effects in the upper area of the electrode, which were observed during pilot operation.

VI. CONCLUSION AND PERSPECTIVES

Different analysis steps (see Figure 2) presented in this paper enable the development of the first industrial magnetohydrodynamic copper slag-cleaning furnace in terms of geometry, electrical power and process parameters.

For the industrial-type reactor design, the conventional reduction furnace (SAF) for slag cleaning must be supplemented by the externally applied magnetic field (electromagnet). In order to represent, for the first time, the electromagnetic conditions for the industrial reactor design, a coupled CFD model is setup, which together with the pilot test results enabled conclusions to be drawn about the reaction kinetics and copper recovery for the mass and energy balance. Numerical back-coupling between the flow field (in FLUENT) and the electromagnetic field (in ANSYS) is required in order to take into account real feedback effects; for the first time, this considers "artificially" generated Lorentz forces in a conventional slag-cleaning furnace.

The major advantage of numerical calculations was that parameters could be freely varied and in post-processing, for example, the flow lines could be displayed spatially as desired in order to determine an optimal flow pattern matched to the industrial reactor geometry. A special challenge in geometry modeling was to choose the correct boundary conditions and material properties (*e.g.*, magnetic permeability number). For this reason, several series of measurements were conducted to determine the magnetic field pattern, which are shown in Figure 7. The material properties of slag and copper matte were taken mainly from basic laboratory-scale experiments and are continuously matched to the simulations results across all pilot test series.

Together with the pilot test evaluation and extrapolation of the different process parameters (*e.g.*, magnetic flux density and power distribution), it has been possible to improve and increase the efficiency of the MHD stirring effect by the external magnet based on the industrial furnace geometry. A comparison of Figure 15(d) with Figure 18(b) shows that at 10 Gauss in the reactor core and with the appropriate electrode current intensity ($I > 20$ kA), the required slag velocity is easily achieved in a conventional rectangular slag-cleaning furnace, enabling optimal reactor volume utilization and eliminating stagnant liquid zones in the upper part of the reactor.

In a next step, it must be analyzed how the change in the direction of the slag movement affects the particle mass transport, the slag reduction rate, and consequently, the coalescence of the copper inclusions. This should be investigated in additional field tests to produce further process parameters for industrial applications.

In conclusion, the numerical research results of the present work for the first MHD copper slag cleaning-process, together with the investigations on the pilot plants, enabled the development of the scientific functional chain "electromagnetic field—MHD flow field—slag properties—metal recovery" in an industrial slag-cleaning reactor. Consequently, the investigation of the physical principles of the MHD cleaning effect on non-ferrous slags has been shown and elaborated.

ACKNOWLEDGMENTS

The authors would like to thank the German Federal Ministry of Education and Research (BMBF) for the funding (Project name: Prevention of Metal Losses in Metallurgical Slags Using the Example of Copper Extraction; Funding codes: BMBF 033R006B; Funding program: Innovative Technologies for Resource Efficiency—Raw Material Intensive Production Processes.) and all project participants (such as Aurubis AG in Hamburg and RWTH Aachen University at the Institute for Metallurgical Process Technology and Metal Recycling) for the excellent cooperation and the project results. Special acknowledgement goes to Prof. A. Warczok and his team at the Department of Mining Engineering at the Universidad de Chile, in Santiago who contributed the essential process principles of magnetohydrodynamic slag cleaning. Personally, my greatest thanks go to Franziska Wichelmann, who has always given me extraordinary support during my work.

CONFLICT OF INTEREST

On behalf of all authors, the corresponding author states that there is no conflict of interest.

FUNDING

Open Access funding enabled and organized by Projekt DEAL.

OPEN ACCESS

NOMENCLATURE

$\underset{\rightarrow}{\Delta}\mathrm{Cu}_i$	Average Cu-separation [wt pct]
$\vec{A}$	ANSYS: vector potential inside each finite element
w_i	ANSYS: vector shape function
α_i	ANSYS: placement function
$\overrightarrow{q_i}$	ANSYS: edge direction
$q\ (r,t)$	ANSYS: field quantity
$c(r)$	ANSYS: measurable field at $\omega t = 0$ deg
$s(r)$	ANSYS: measurable field at $\omega t = -90$ deg
ω	ANSYS: angular frequency of time change[deg]
r	ANSYS: location vector in space [m]
t	Time [s]
F^{jb}	ANSYS: Lorentz force density
$J_{r/i}$	ANSYS: current density—real and imaginary component
$B_{r/i}$	ANSYS: magnetic flux density—real and imaginary component
Q^i	ANSYS: Joule power density heating per unit volume
$E_{r/i}$	ANSYS: electric field intensity—real and imaginary component
$\vec{v}$	FLUENT: velocity [m/s]
p	FLUENT: pressure [N/m^2]
v	FLUENT: kinematic viscosity [Pa s]
F	Lorentz force [N]
$\rho_{S/M}$	Slag and matte density [kg/m^3]
$\eta_{S/M}$	Slag and matte viscosity [Pa s]
σ	Electrical conductivity [1/Ωm]
k	Thermal conductivity [W/m K]
c_p	Thermal capacity [J/kg K]
$\beta_{S/M}$	Slag and matte coefficient of thermal expansion [1/K]
μ	Magnetic permeability [Vs/Am]
μ_r	Relative permeability [–]
I	Electrode current [kA]
B	Magnetic flux density [Gauss]
$V_{max/avg}$	Maximal and average flow velocity [m/s]
U	Bath voltage [Volt]

REFERENCES

1. D. Kupferinstitut: *Herstellungsverfahren -Herstellungsverfahren*, 2004, vol. 1, pp. 6–14.
2. K. H. Bruch, D. Gohlke, C. Kögler, J. Krüger, M. Reuter, I.v. Röpenack, E. Rombach, G. Rombach, P. Winkler: Sachbilanz einer Ökobilanz der Kupfererzeugung und -verarbeitung, Institut für Metallhüttenwesen und Elektrometallurgie der RWTH Aachen, 1995, vol. 1, 2, and 3, no. 4, 5, and 6.
3. R. König, M. Deres, T. Töpfer: Vermeidung von Metallverlusten in metallurgischen Schlacken am Beispiel der Kupfergewinnung, 2013, BMBF 033R006.
4. A. Warczok, G. Riveros, T. Marin, R. Degel, J. Kunze, H. Oterdoom, and T. Wuebbels: *The Carlos Díaz Symposium on Pyrometallurgy Cu*, 2007, vol. 3, pp. 351–65.
5. A. Warczok and G. Riveros: *Miner. Eng.*, 2006, vol. 20, pp. 34–43.

6. V. Bojarevičs, J.A. Freibergs, E.I. Shilova, E.V. Shcherbinin: Electrically Induced Vortical Flows, in: Mechanics of Fluids and Transport Processes, 1989, vol. 9, pp. 18–62.
7. A. Kharicha, M. Al-Nasser, H. Barati, E. Karimi-Sibaki, A. Vakhrushev, M. Abdi, A. Ludwig, and M. Wu: *Eur. J. Mech. B*, 2022, vol. 94, pp. 90–105.
8. A. Kharicha, A. Alemany, and D. Bornas: *Int. J. Heat Mass Transf.*, 2004, vol. 47, pp. 1997–2014.
9. K. Messadek and R. Moreau: *J. Fluid Mech.*, 2002, vol. 456, pp. 137–59.
10. J. Sommeria: *J. Fluid Mech.*, 1988, vol. 189, pp. 553–69.
11. J. Sommeria: Nouveaux Aspects. Les Houches - Ecole D'Ete de Physique Theorique, 2001, vol. 74. pp. 1–25.
12. A. Kharicha, E. Karimi-Sibaki, M.H. Wu, A. Ludwig, and J. Bohacek: *Steel Res. Int.*, 2018, vol. 89(1), pp. 170–200.
13. O. Kazak: *Metall. Trans. B*, 2013, vol. 44B, pp. 1243–250.
14. H. Barati, A. Kharicha, M. Al-Nasser, D. Kreuzer, G. Hackl, M. Gruber, A. Ishmurzin, C. Redl, A. Teplyakov, and I. Ludwig: *J. Phys. Commun.*, 2022, vol. 6, pp. 1–2.
15. K. Liu, F. Stefani, N. Weber, T. Weier, and B.W. Li: *Magnetohydrodynamics*, 2020, vol. 56(1), pp. 27–42.
16. I. Kolesnichenko, P. Frick, V. Eltishchev, S. Mandrykin, and F. Stefani: *Phys. Rev. Fluids*, 2020, vol. 5, 123703.
17. M. Choudhary and J. Szekely: *Metall. Trans. B*, 1980, vol. 11, pp. 439–53.
18. A. Jardy, D. Ablitzer, and J.F. Wadier: *Metall. Trans. B*, 1991, vol. 22B, pp. 111–20.
19. Y.Y. Sheng, G.A. Irons, and D.G. Tisdale: *Metall. Trans. B*, 1998, vol. 29B, pp. 77–83.
20. Y.Y. Sheng, G.A. Irons, and D.G. Tisdale: *Metall. Trans. B*, 1998, vol. 29B, pp. 85–94.
21. L.H. Gunnewiek, S. Tullis: Proceedings of the International Symposium on Computational Fluid Dynamics and Heat/Mass Transfer Modelling in the Metallurgical Industry, 1996, pp. 250–264.
22. L.H. Gunnewiek, L. Oshinowo, T. Plikas, R. Haywood: Tenth International Ferroalloys Congress, INFACON X, 2004, pp. 555–564.
23. T. D. Hadley, H.P. Kritzinger, I. McDougall, E. Prinsloo, D.S. Van Vuuren: Assessment of Polokwane Furnace cooler failure, CSIR South Africa, 2006.
24. U. Krieger, B. Halbedel, D. Hülsenberg, and A. Thess: *Eur. J. Glass Sci. Technol. A*, 2008, vol. 49, pp. 33–40.
25. D. Hülsenberg, B. Halbedel, G. Conrad, A. Thess, Y. Kolesnikov, and U. Lüdtke: *Glass Sci. Technol.*, 2004, vol. 77, pp. 186–93.
26. C. Gießler, C. Sievert, U. Krieger, B. Halbedel, D. Hülsenberg, U. Lüdtke, and A. Thess: *Fluid Dyn. Mater. Process.*, 2005, vol. 1(3), pp. 247–66.
27. D. Cepite, A. Jakovics, B. Halbedel, and U. Krieger: *The international journal for computation and mathematics in electrical and electronic engineering*, 2008, vol. 27(2), pp. 387–98.
28. J. Perez: *Dissertation*, Technische Universität Illmenau, Fakultät für Maschinenbau, 2016.
29. A. Warczok.: SAF Fundamentals, Stage I Manual, Universidad de Chile, 2003.
30. A. Warczok: *SAF Fundamentals*, Universidad de Chile, Mathematical Model of Copper Slag Cleaning Manual, 2003.
31. C. Caballero, A. Moyano, F. Rojas, J. Font, A. Warczok: 8th International Conference on Molten Slags, Fluxes, and Salts, 2009, pp. 1221–1230.
32. V.B. L'vov: *Thermochim. Acta*, 2000, vol. 320, pp. 109–20.
33. L. Li, H. Wang, J-H. Hu: 2010 International Conference on Digital Manufacturing & Automation, 2010, vol. 2, pp. 823–835.
34. T. Oishi, M. Kamuo, K. Ono, and J. Moriyama: *Metall. Trans. B*, 1983, vol. 14B, pp. 101–04.
35. V.G. Levich: *Physicochemical Hydrodynamic*, Prentice-Hall Inc, Hoboken, 1962, pp. 472–531.
36. S. Itoh, R.T.C. Choo, and J.M. Toguri: *Can. Metall. Q.*, 1995, vol. 34(4), pp. 319–30.
37. U.C. Andres, L.S. Poliak, and S.I. Sirovatskij: *Zurnal Techniceskoj Fiziki*, 1963, vol. 33(3), pp. 334–42.
38. D. Leenov and A. Kolin: *J. Chem. Phys.*, 1954, vol. 22, pp. 683–88.
39. A. Warczok and G. Riveros: *Report*, Pilot Industrial Test in Chagres Smelter, Universidad de Chile, Electrodynamic Slag Cleaning, 2007.
40. A. Warczok, G. Riveros, R. Degel, J. Kunze, M. Kalisch, H. Oterdoom: Proceedings Copper2010, 2010, vol. 3, pp. 1213–1231.
41. R. König, A. Weyer, R. Degel, J. Schmidl, H. Kadereit, A. Specht: REWAS 2013 Enabling Materials Resource Sustainability, 2013, pp. 2–12.
42. R. König, R. Degel, H. Oterdoom, J. Schmidl, H. Kadereit, A. Specht, A. Warczok: Nickolas Themelis Symposium on Pyrometallurgy and Process Engineering Copper2013, 2013, vol. 3, pp. 195–206.
43. J.M. Floyd, P.J. Mackey: Extraction Metallurgy '81, 1981, pp. 345–371.
44. A. Jha and P. Grieveson: *Scand. J. Metall.*, 1992, vol. 21, pp. 50–62.
45. N. Cardona, P. Coursol, J. Vargas, and R. Parra: *Can. Metall. Q.*, 2011, vol. 50(4), pp. 318–29.
46. J. Kunze, R. Degel, D. Borgwardt, A. Warczok, G. Riveros: Method and device for extracting a metal from slag containing the metal, WO2006/131372 A1, 2006.
47. ANSYS FLUENT: FLUENT 6.3 User's Guide, 2006.
48. ANSYS: Release 11.0 Documentation for ANSYS, 2006.
49. W. Schätzing: FEM für Praktiker – Band 4: Elektrotechnik, Renningen, Expert Verlag, 2003, vol. 3.
50. ANSYS Release 11.0: Low-Frequency Electromagnetic Analysis Guides, 2014.
51. C. A. Snyders: Master thesis, Department of Process Engineering at Stellenbosch University, 2008.
52. A. Warczok: Report, Fluiddynamic and Heat Transfer Modeling of Slag Cleaning in an Electric Furnace, Universidad de Chile, 2003.
53. J. Otto, M. Hanke: Magnetic Field Simulation, Seminar document, ANSYS Competence Center FEM, CADFEM, 2010.